The structure and lifecycle of stratified mixing by shear instabilities in continuously forced flows

Adrien Lefauve[1], Christopher S Bassett[2], Daniel Plotnick[3], Andone Lavery[4], and W Rockwell Geyer[5]

[1]Imperial College London
[2]University of Washington
[3]Pennsylvania State University
[4]Oregon State University
[5]Woods Hole Oceanographic Institution

December 26, 2025

Abstract

The turbulent energy cascade of ocean mixing remains poorly understood because of the wide separation of scales at high Reynolds numbers (Re). Here we propose a new conceptual model for the structure of small-scale mixing grounded in high-resolution multibeam echosounding observations from the mouth of the Connecticut River, a shallow salt-wedge estuary. Tidal forcing and bottom topography slope the pycnocline, sustaining interfacial shear and Kelvin–Helmholtz instabilities well below the marginal instability threshold on a vertical scale of order 1 m. Acoustic backscatter, used here as a proxy for salinity microstructure dissipation, provides time-resolved, two-dimensional imagery of the true structure and evolution of turbulent mixing. At Re˜10ˆ6, we find that mixing is dominated not by the collapse of slowly evolving billow cores as at Re˜10ˆ3-10ˆ4, but instead by fast turbulence within the ˜10 cm thin, shallow-sloping braids that connect them, energized by baroclinic shear. We explain these observations using two-dimensional direct numerical simulation at field-matched parameters, which predicts the emergence of secondary Kelvin–Helmholtz instabilities and turbulence within the braids, pre-empting further steepening and primary overturn. Laboratory experiments in an inclined duct, used as an analogue of the turbulent braid regime, provide estimates and visualizations of mixing down to the dissipative scales, where it remains organized in myriad thin, sheared filaments rather than overturns. We conclude that high-Re mixing hotspots sustained by baroclinic shear forcing follow fundamentally different dynamics than previously thought.

The structure and lifecycle of stratified mixing by shear instabilities in continuously forced flows

Adrien Lefauve[1,2], C. Bassett[3], D. S. Plotnick[4], A. C. Lavery[5] and W. R. Geyer[6]

[1]Grantham Institute – Climate Change and the Environment, Imperial College London, UK
[2]Department of Civil and Environmental Engineering, Imperial College London, UK
[3]Applied Physics Laboratory, University of Washington, Seattle, WA, USA
[4]Applied Research Laboratory, Pennsylvania State University, PA, USA
[5]College of Earth, Ocean and Atmospheric Sciences, Oregon State University, OR, USA
[6]Applied Ocean Physics and Engineering Department, Woods Hole Oceanographic Institution, MA, USA

Abstract

The turbulent energy cascade of ocean mixing remains poorly understood because of the wide separation of scales at high Reynolds numbers (Re). Here we propose a new conceptual model for the structure of small-scale mixing grounded in high-resolution multibeam echosounding observations from the mouth of the Connecticut River, a shallow salt-wedge estuary. Tidal forcing and bottom topography slope the pycnocline, sustaining interfacial shear and Kelvin–Helmholtz instabilities well below the marginal instability threshold on a vertical scale of order 1 m. Acoustic backscatter, used here as a proxy for salinity microstructure dissipation, provides time-resolved, two-dimensional imagery of the true structure and evolution of turbulent mixing. At $\mathrm{Re} \sim 10^6$, we find that mixing is dominated not by the collapse of slowly evolving billow cores as at $\mathrm{Re} \sim 10^3 - 10^4$, but instead by fast turbulence within the ~ 10 cm thin, shallow-sloping braids that connect them, energized by baroclinic shear. We explain these observations using two-dimensional direct numerical simulation at field-matched parameters, which predicts the emergence of secondary Kelvin–Helmholtz instabilities and turbulence within the braids, pre-empting further steepening and primary overturn. Laboratory experiments in an inclined duct, used as an analogue of the turbulent braid regime, provide estimates and visualizations of mixing down to the dissipative scales, where it remains organized in myriad thin, sheared filaments rather than overturns. We conclude that high-Re mixing hotspots sustained by baroclinic shear forcing follow fundamentally different dynamics than previously thought.

Plain Language Summary

The mixing of different water layers in the ocean is not well understood, despite being central to how the ocean moves and breathes. This is partly because the process driving mixing – turbulence – spans an enormous range of scales, from kilometers down to microns, making it hard to connect real-world observations with computer models. Intense mixing happens in 'hotspots' created by strong flows, such as tides in estuaries. Here we introduce a new model for such mixing based on high-resolution multibeam sonar data from the Connecticut River estuary. Unlike conventional single-beam sonar, the multibeam gives images that show the true shapes of underwater waves and their thin, fast-moving braids. These braids act like the steep face a surfer rides, but we show that underwater waves rarely steepen sufficiently to form a 'roller' at their crest. Instead, the slopes of the braids spawn many smaller breaking waves that do the mixing. Computer simulations mimicking the observations confirm this scenario, and laboratory experiments in a sloping channel let us zoom in on this braid mixing. Our results differ from smaller-scale waves, where mixing is found inside the main rollers, and could improve predictions in other vigorous zones, including in the coastal and open-ocean.

1 Introduction

Diapycnal turbulent mixing is one of cornerstones of ocean dynamics. The way mixing regulates the vertical transport and thus the distribution of active scalars (e.g. temperature, salinity) and passive scalars (e.g. carbon, nutrients) has far-reaching implications for ocean and climate physics (Melet et al., 2022). Since the ocean is mostly stably-stratified, small-scale turbulence is often initiated by shear instabilities – typically Kelvin-Helmholtz instabilities – triggered when the local shear $S = |\partial u/\partial z|$ exceeds twice the buoyancy frequency $N = \sqrt{\partial b/\partial z}$, i.e. when the gradient Richardson number satisfies

$$\mathrm{Ri_g} = \frac{N^2}{S^2} < \frac{1}{4}, \tag{1}$$

which is referred to as the Miles-Howard criterion (Miles, 1961; Howard, 1961). These instabilities, and the stratified turbulence that ensues, are the key energy pathway between submesoscales (above 100 m or so) and three-dimensional turbulence (below 0.1 m or so) (Smyth & Moum, 2012; D'Asaro, 2022; Taylor & Thompson, 2023).

Certain environments are continually forced, i.e. both the vertical buoyancy contrast and the shear are sustained, leading to frequent cycles of shear instabilities. These hotspots include straits (Wesson & Gregg, 1994), the equatorial undercurrent (Smyth et al., 2013), deep overflows (Cusack et al., 2019), deep seamounts (van Haren & Gostiaux, 2010), shallow seamounts (Vladoiu et al., 2025) and estuaries (Geyer et al., 2010). These hotspots not only contribute to large-scale water mass transformation and energy budgets (Cimoli et al., 2023; Waterhouse et al., 2014) but also shape local circulation patterns, chemistry and biology (Steinbuck et al., 2009; Hoecker-Martínez & Smyth, 2012; Hasegawa et al., 2021) and can feed back on climate modes such as the El Niño–Southern Oscillation (Liu et al., 2025) due to their high levels of turbulent kinetic dissipation ϵ and mixing χ, defined as

$$\epsilon = 2\nu\,||\mathbf{s}||^2 \quad \text{and} \quad \chi = 2D\,|\nabla b|^2. \tag{2}$$

Here $\mathbf{s} = (\nabla\mathbf{u} + \nabla\mathbf{u}^T)/2$ is the strain rate tensor from the three-dimensional velocity field $\mathbf{u}$, ν is the kinematic viscosity of seawater, and D is the molecular diffusivity of the buoyancy field b due to salinity or temperature variations. In addition to being energetically important, these continuously forced environments are ideal to study shear instabilities. Understanding their spatial structure and temporal evolution (lifecycle) is crucial to build physics-based parameterizations of their non-hydrostatic effects in regional and global ocean models.

Yet, despite their importance, detailed observations of shear instabilities remain relatively rare. We show in figure 1 one of the highest-resolution observations to date, which will be analyzed in more detail in this paper. Figure 1(a) shows a 300 m long transect at the mouth of the Connecticut River, along the thalweg, where shear is sustained between the surface river discharge and the incoming flood tide. This transect was collected by an echosounder in an autonomous underwater vehicle (AUV) (Remote Environmental Monitoring UnitS, REMUS) cruising 1 m below the surface. The signal displayed is acoustic volume scattering strength, which is directly proportional to the logarithm of the turbulent dissipation of salinity variance $\log_{10}\chi_s$ ((Lavery et al., 2013); details in Sec. 4). Figure 1(b-c) zooms in on shear instabilities on various scales revealed by the backscatter. This paper will focus on the large-scale instabilities found in the mid-water column at the main pycnocline, shown in figure 1(c). This train of KH instabilities grows spatially along the direction of the mean flow from right to left. It appears to be triggered by a tidal intrusion front (Simpson & Nunes, 1981) following the bottom slope of 0.02 (see panel a) and displays an identical mean slope of 0.02 (panel c). (The smaller, steeper train of KH instabilities in panel b appears at the edge of a near-surface shear layer.) The

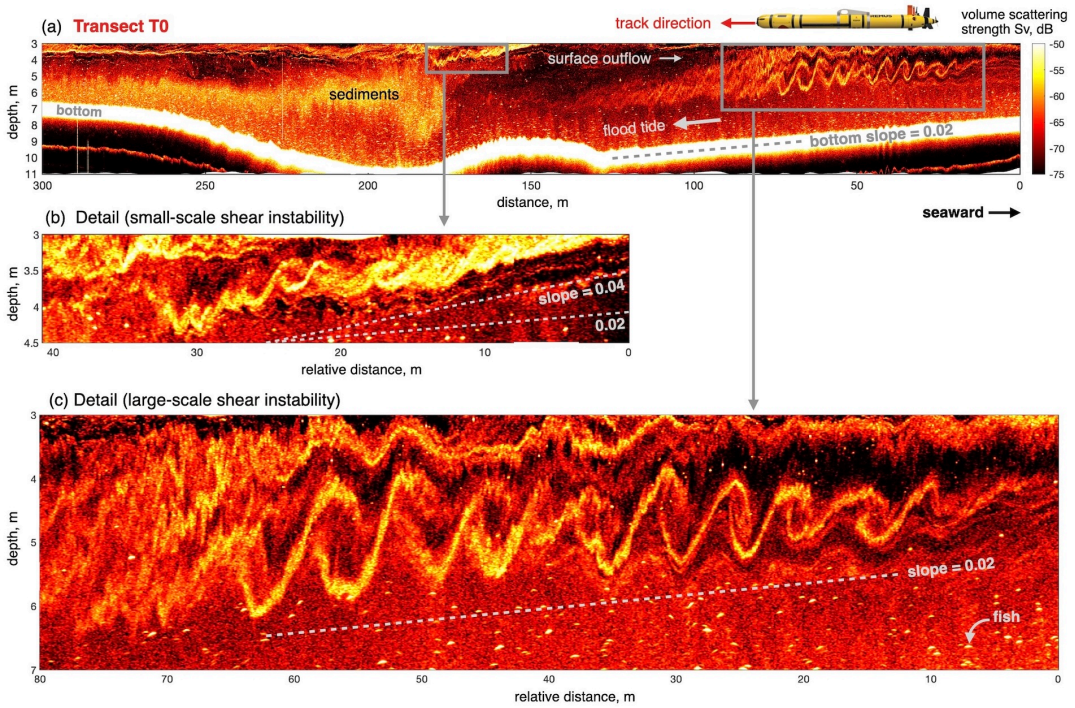

Figure 1. Visualisation of turbulent mixing caused by shear instabilities from the acoustic backscatter acquired by an Underwater Autonomous Vehicle in the Connecticut River estuary. (a) Whole transect T0 (further details in figures 2 and 3). (b-c) Zooming in on details of small-scale (b) and large-scale (c) trains of KH instabilities, the latter one being the main focus on this paper. The vertical exaggeration is 5 in all panels (real slopes are much shallower). The spatial resolution is of order 1 cm in depth and 8 cm along transect. The small bright spots are fish, particularly abundant in the salty bottom layer.

bright coherent yellow signal in panel (c) indicates regions of elevated turbulent mixing caused, as discussed in Sec. 4.

Such observational data inform us about where and when energy dissipation and its associated mixing are strongest. Until now, this understanding was built largely from direct numerical simulations (DNS) (e.g. (Smyth & Moum, 2000; Mashayek & Peltier, 2011)) and laboratory experiments (e.g. (Thorpe, 1971, 1973)) at moderate Reynolds numbers $\mathrm{Re} = UH/\nu \sim 10^3$–$10^4$, where U and H are representative velocity and length scales. At these Re, the KH billows grow, break turbulently, mix, and then decay due to the lack of forcing. By contrast, the oceanic regime in figure 1 has a higher $\mathrm{Re} \sim 10^6$ and is continuously forced. This is significant for two reasons. First, Re controls the transition to turbulence and the emergence of smaller secondary instabilities (Caulfield & Peltier, 2000; Mashayek & Peltier, 2012a), which set the turbulent length scales and the history of mixing (Caulfield, 2021). Second, forcing controls the energetics: in continuously forced stratified shear flows – and in other dissipative systems governed by a threshold (here $\mathrm{Ri_g} = 1/4$) – the rates of kinetic energy and buoyancy variance dissipation (ϵ and χ) balance, on average, the input rates (solar heating and trade winds for the equatorial undercurrent; high-latitude cooling and downslope motion for deep overflows; freshwater discharge and tides for estuaries). Shear continuously destabilizes the flow by decreasing $\mathrm{Ri_g}$ below the threshold, while turbulent events restore stability by increasing $\mathrm{Ri_g}$, producing cycles around an equilibrium value – the state of marginal instability (Thorpe & Liu, 2009; Smyth, 2020) or self-organized criticality (Bak et al., 1988; Salehipour et al., 2018).

Evidence already exists that the moderate-Re, unforced DNS regime differs from the high-Re, forced regime in the ocean. In DNS, most of the mixing occurs within the convectively unstable billows ("bright cores"), whereas field observations at Re $\sim 10^6$ (see figure 1c and Appendix A) show that mixing concentrates instead in the connecting "bright braids" – thin, high-shear regions linking the weaker "quiet cores". In this paper, we confirm this hypothesis and turn it into a predictive model by addressing two major open questions tied to long-standing methodological challenges.

(1) What are the spatial structure and lifecycle of these high-mixing zones? Most existing backscatter data, including that shown in figure 1 and Appendix A, comes from *single-beam* echosounders, meaning that vertical soundings (lines) are aggregated along the track axis, creating two-dimensional images which inevitably suffer from distortions associated with the relative motion between the underwater KH wave (controlled by the depth-varying current) and the instrument. This can either steepen or flatten slopes, and generally entangles spatial and temporal evolutions in ways that are hard to quantify and correct for. Here we overcome this challenge with a *multibeam* echosounder that disentangles spatial and temporal evolution and captures the fine-scale dynamics of shear-instability mixing down to centimeter scales and tens of milliseconds.

(2) How does the turbulent cascade operate within these high-mixing braids, well below the resolution of direct observations, down to sub-mm scale? The high Re values in the ocean allow the KH braids to sharpen down to the cm scale and increase their local shear, triggering secondary instabilities and turbulence. We will use highly-resolved two-dimensional (2D) DNS with parameters matching field values to demonstrate this process and quantify the length- and time-scales involved. After the emergence of three-dimensional (3D) braid turbulence at scales of ~ 10 cm, theory predicts a downscale cascade with an multi-decade inertial range. We will use insight from 3D experimental data obtained in a relevant laboratory apparatus to visualise mixing down to scales of 0.1 mm, and quantify the energetics of turbulence forced by the braid slope. This will allow us to hypothesize why the primary cores rarely have the time to overturn in observations, completing our understanding of the structure and lifecycle of mixing by shear instabilities in continuously forced flows.

To answer these questions, Sec. 2 introduces the observational data, including the field site, instruments, and multibeam echosounding. In addition to the AUV transect from figure 1, three ship-board transects with co-located acoustics and hydrodynamic data will reveal in Sec. 3 the forcing mechanism leading to the primary KH instability and the expected separation of scales of turbulence, motivating the next sections. Sec. 4 delves deeper into the acoustics data, documenting the features of braid turbulence with the multibeam data and comparing them to the single-beam data of figure 1. Sec. 5 employs numerical modeling to prove the existence of and characterize secondary braid instabilities before explaining how existing laboratory experiments in an inclined flume are relevant to probe the ensuing braid turbulence. Sec. 6 concludes and Sec. 7 gives the broader implications of our findings for ocean mixing.

2 Methods and overview of observations

2.1 Site and instruments

We conducted field observations at the mouth of the Connecticut River estuary (figure 2a-b), focusing on a study region with a natural channel 5–10 m deep with gently sloping bathymetry (figure 2c). The dataset comprises four transects which exhibit a large number of KH instabilities: T0, surveyed with an autonomous underwater vehicle (AUV), already shown in figure 1, and T1–T3, obtained from shipboard measurements. The instrumentation is summarized in figure 3. The AUV (model: REMUS 100) carried a broadband single-beam echosounder oper-

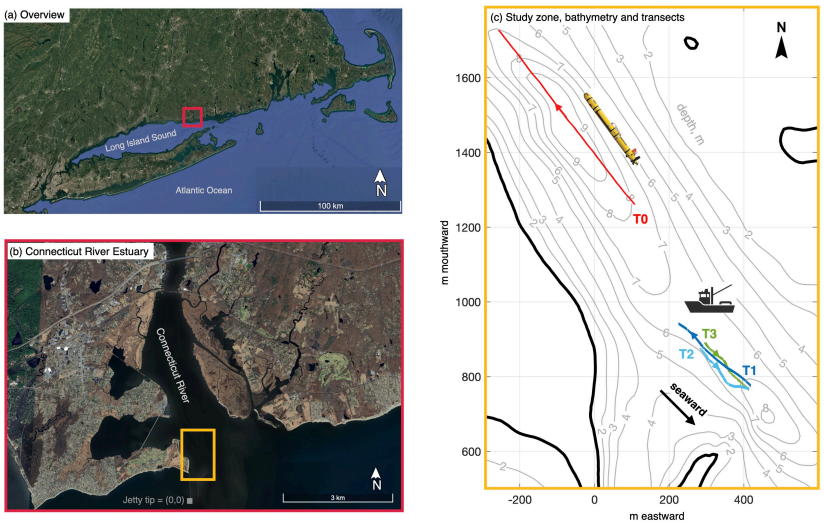

Figure 2. Field site. (a) Location of the Connecticut River estuary (see red box). (b) Zoom in on the mouth of the estuary. Note the study zone (see yellow box) and the jetty tip as reference point with coordinates $(0, 0)$. (c) Bathymetry and transects in the study zone (coordinates are relative to the jetty tip). The four transects investigated in this paper: T0 (AUV-based) and T1-3 (shipboard).

ating at 200 kHz nominal frequency (model: Simrad WBTmini with ES200-7CDK transducer, 7° full beamwidth, 100 kHz bandwidth, 1 ms signal) (Bassett et al., 2022). The vessel mounted equipment included a pole mounted off the starboard side with (i) a multibeam echosounder (Kongsberg M3) operating at 500 kHz with a 20 μs pulse with a nominal resolution of 1.5 cm (Melvin et al., 2012); (ii) a co-located acoustic Doppler current profiler (ADCP) providing current data at 0.25 m vertical resolution (Nortek Signature 1000, operating at 1 MHz); and (iii) a towed array of five conductivity–temperature–depth (CTD) sensors spaced 1 m vertically (RBR Concerto, sampling at 17 Hz). Unlike conventional multibeam systems, which are typically oriented cross-track to image the seafloor, ours aligned the transmit–receive swath in the along-track direction, parallel to the vessel's motion (figure 3b). This fore–aft geometry captured the instabilities along the vessel's path (following the thalweg) in the plane in which they develop and evolve. The raw multibeam data were rectified to correct for vessel heave, pitch, and roll by combining navigation and motion-sensor data with feature tracking using backscattering from the seabed (for details, see Supporting Information Text S1). This fine level of multibeam data motion correction is essential for the visualization and interpretation of small-scale coherent structures that follows since even modest changes (e.g. several degrees) in pitch and roll associated with unavoidable vessel motion can significantly shift the apparent location of imaged features.

The T0 data were collected on 29 June 2017 (between 16:18:57 - 16:23:52 UTC, local time = UTC-4), approximately 3.5 hours after slack water (12:55 UTC), during the flood tide. The AUV was cruising 1 m below the surface at a constant speed of $1\,\mathrm{m\,s^{-1}}$. The T1-3 data were collected a day later on 30 June 2017 (16:05:30 - 16:33:21 UTC), approximately 2-2.5 hours after slack water (14:05 UTC), also during the flood tide. The vessel speed varied during each transect and between transects, with averages of $1.9\,\mathrm{m\,s^{-1}}$ (T1), $0.45\,\mathrm{m\,s^{-1}}$ (T2) and $0.63\,\mathrm{m\,s^{-1}}$ (T3). Although our data is exclusively during the flood tide, KH instabilities have been previously documented during the ebb tide at the mouth and further upstream (Geyer et al., 2010; Lavery et al., 2013; Holleman et al., 2016; Geyer et al., 2017). This estuary, like many others, is a mixing hotspot because of the combination of strong shear and persistent stratification.

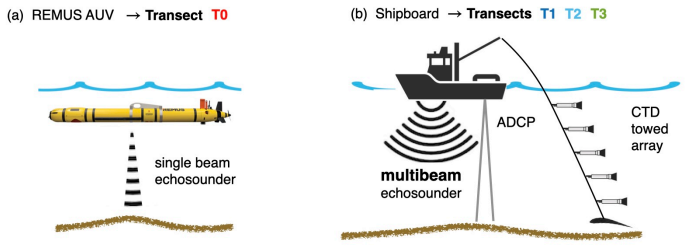

Figure 3. Instrumentation and resulting datasets. (a) The AUV-based transect T0 provide single-beam acoustics. (b) The shipboard transects T1-3 provide multibeam acoustics with current profiles (nearly collocated ADCP) and salinity/density profiles (towed CTD, just aft of the vessel).

In summary, the three shipboard transects (T1–3) provide multibeam acoustic data resolving the structure and lifecycle of shear-instability mixing (details in Sec. 2.2), together with concurrent current and salinity profiles used to examine the background conditions, forcing, and characteristic turbulent length-scales (Sec. 2.3 and 3).

2.2 Acoustic backscatter as a proxy for turbulent mixing

The backscatter measured by our echosounders arises from scattering by fine-scale salinity microstructure. (Lavery et al., 2013) developed an analytical model – validated by measurements in the Connecticut River estuary – that links the scattering to the rate of salinity mixing χ_s. This relation assumes a turbulent spectrum in the viscous–convective subrange and a mixing efficiency, and it predicts that the volume backscattering cross section per unit volume at a fixed frequency can be expressed as:

$$\sigma_V = C_1\,\chi_s\,\epsilon^{-1/2} = C_1\,\frac{\Gamma^{1/2}}{g\beta}\chi_s^{1/2} \qquad \text{where} \quad \Gamma = \frac{\chi}{\epsilon} = \frac{(g\beta)^2\chi_s}{\epsilon}. \tag{3}$$

In the above, C_1 is a constant at a fixed acoustic frequency, Γ is the mixing efficiency, i.e. the ratio between dissipation of buoyancy variance $\chi = (g\,\beta)^2\chi_s$ and kinetic energy dissipation ϵ (Caulfield, 2020, Eq. 10), and β is the saline contraction coefficient ($\beta = 7.5\times10^{-4}\,\mathrm{psu}^{-1}$ at our temperature of 20 °C). Assuming a constant mixing efficiency Γ, the volume backscatter cross section simplifies to $\sigma_V = C_2\,\chi_s^{1/2}$, where C_2 is another constant.

In this paper we follow sonar acoustics convention and present results in terms of the volume backscattering strength S_V (units dB re 1 m^{-1}):

$$S_V = 10\log_{10}\sigma_V = 5\log_{10}\chi_s + C_3, \tag{4}$$

where C_3 is another constant whose determination would require calibration. Calibration was performed in (Lavery et al., 2013) but not in this work due to challenges with in situ calibrations of multibeam systems. Thus, direct inversions of S_V for χ_s is not possible and there is a scalar offset between the values of S_V presented here and those of calibrated systems. However, the essential point here is that a tenfold increase in the underlying mixing rates χ_s and χ corresponds to a 5 dB increase in the measured S_V. In our data, S_V spans a range of about 20 dB, implying four orders of magnitude variation in χ_s. This inferred dynamic range is consistent with previous observations using a calibrated single-beam system; (Lavery et al., 2013, figure 16b) reported a range $\chi_s \approx 10^{-3} - 1\,\mathrm{psu}^2\,\mathrm{s}^{-1}$ within shear instabilities in the main pycnocline.

The processed multibeam data $S_V(x,z,t)$ are output at 17 Hz with a nominal grid spacing of 4 mm in the x–z plane. The effective physical resolution, however, is estimated to be closer to

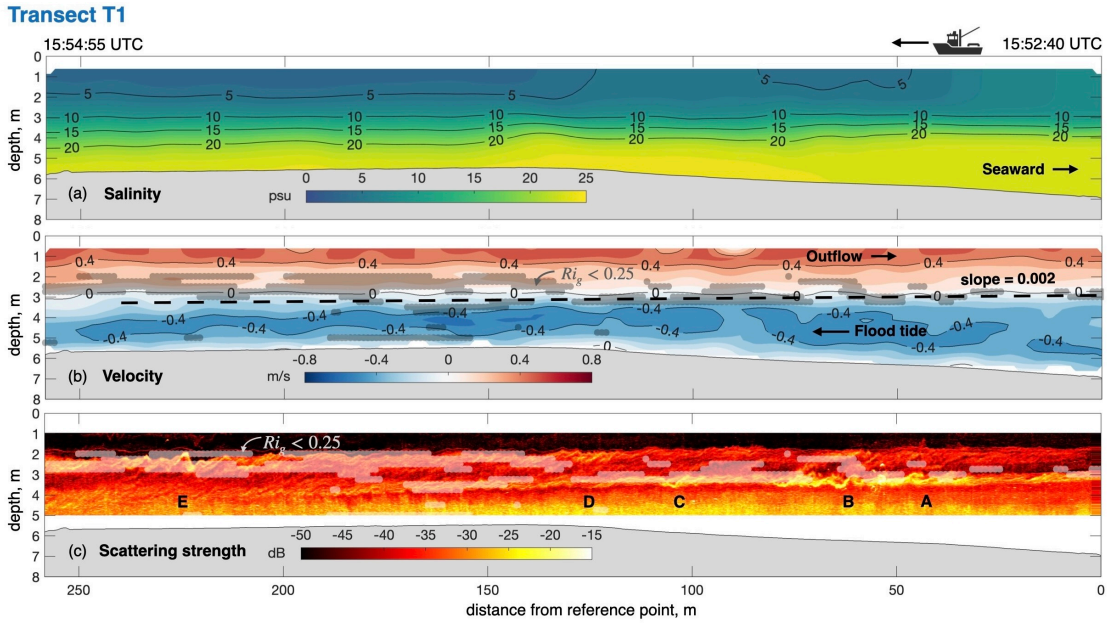

Figure 4. Overview of transect T1, starting 1 h 47 min after slack water. Track direction is right to left (see the horizontal distance axis). The reference point (distance 0) corresponds to the start of T1 and the end of T2 and T3 (see figure 2c). Vertical exaggeration is 5 in all panels. (a) Salinity, fitted from the CTD towed array. (b) Velocity from ADCP (magnitude of the 2D vector $(u^2 + v^2)^{1/2}$). (c) Scattering strength, taking only the vertical beam of the multibeam. Multibeam snapshots are shown at locations labeled A, B, ..., E in figure 9. In (b,c) the grey/white shading denotes where $\mathrm{Ri_g} < 0.25$ and $N > 0.15\,\mathrm{s}^{-1}$, where we expect (and usually find) strong scattering due to turbulent mixing.

1-2 cm in the vertical (Bassett et al., 2023), with slightly finer discrimination in range than in azimuth, especially at depth due to the $\sim 1.6°$ resolution of the fan. In practice, these data can thus confidently resolve structures of order ~ 5 cm, including turbulent braids.

2.3 Shipboard transects overview

The hydrodynamic and acoustic data from transects T1–3 are shown in figures 4–6. In each figure, the top panel (a) presents the salinity along the transect, obtained by fitting a hyperbolic tangent function to the five-point towed CTD array, which yielded excellent fits. The middle panel shows the ADCP velocity profiles, with river discharge plotted as positive velocities (red) and flood tide as negative velocities (blue), consistent with the convention that seaward flow is left to right. The bottom panel (c) displays the volume scattering strength S_V from the vertical beam of the multibeam, providing an overview consistent with the AUV transect of figure 1. Full multibeam fields are presented later for selected snapshots (labeled A, B, C, ...) in figure 9, corresponding to shear instabilities captured at maximum amplitude.

All three transects show a pycnocline sloping slightly upward seaward under the flood tide (figures 4–6a). The corresponding region of strongest shear – and hence expected KH instability – is marked by grey and white semi-transparent dots where $\mathrm{Ri_g} < 0.25$ and $N > 0.15\,\mathrm{s}^{-1}$ (figures 4–6b,c). As the flood tide progresses, the pycnocline and unstable region rise from about 3 m in T1 to 2 m in T3, with a typical slope of ≈ 0.002 (black dashed lines). This region coincides with intense scattering, confirming that mixing occurs where $\mathrm{Ri_g} < 0.25$.

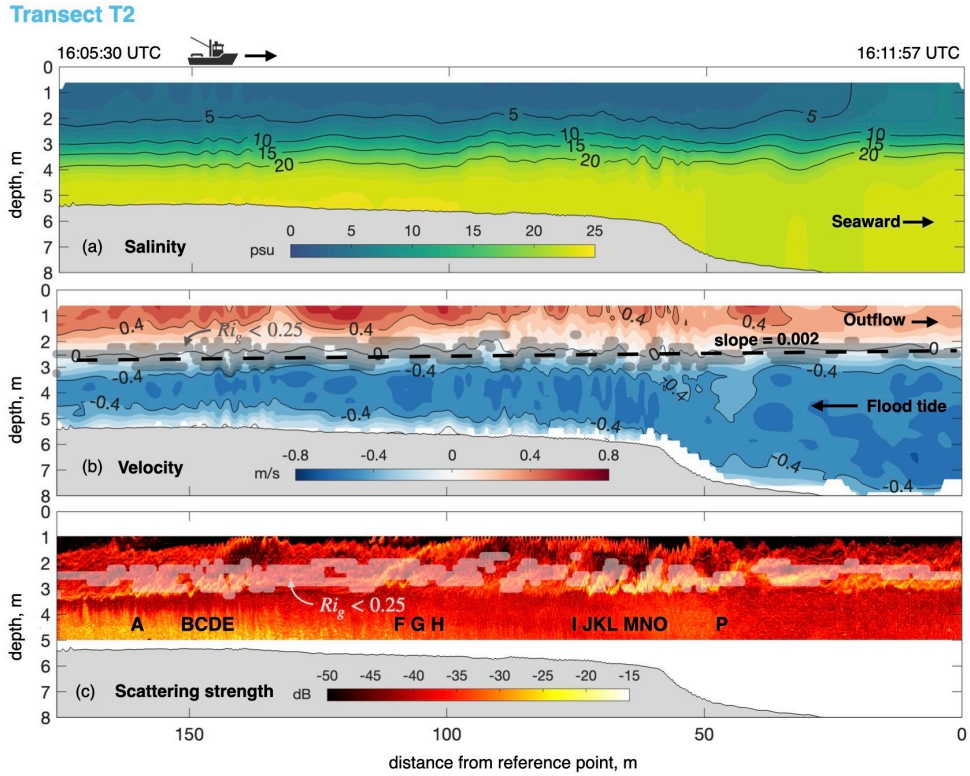

Figure 5. Overview of transect T2, starting 2 h 0 min after slack water. Track direction is left to right (seaward). Same legend as figure 4. Multibeam images are shown at locations A, B, ... P, in figure 9.

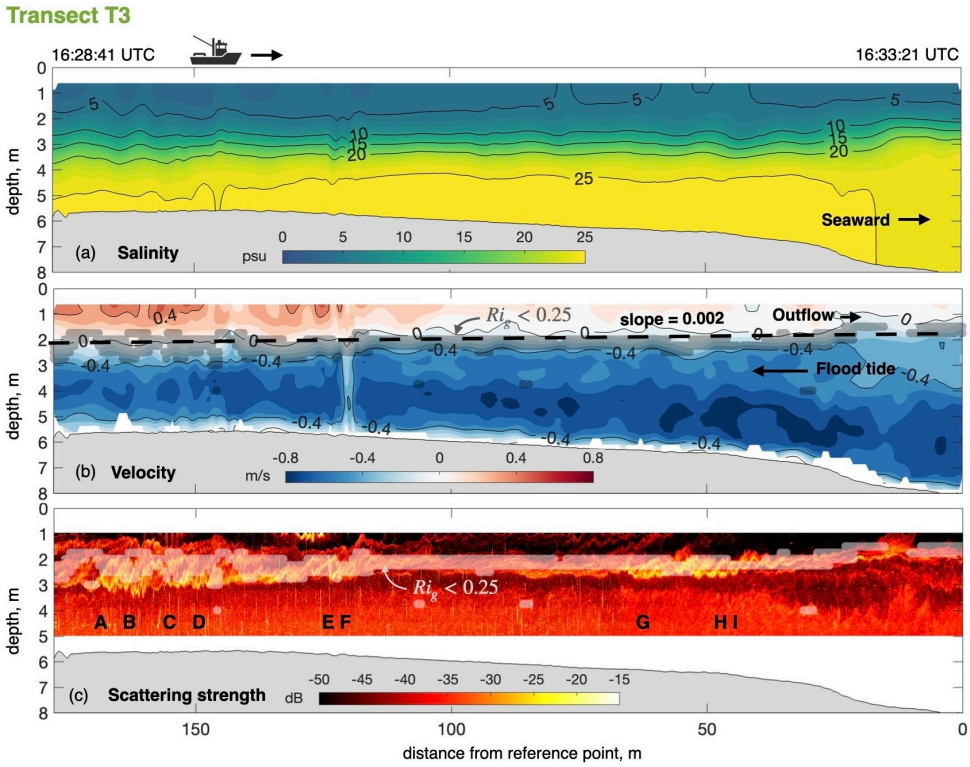

Figure 6. Overview of transect T3, starting 2 h 23 min after slack water. Track direction is left to right (seaward). Same legend as figure 4. Multibeams images are shown at locations A, B, ..., I in figure 9.

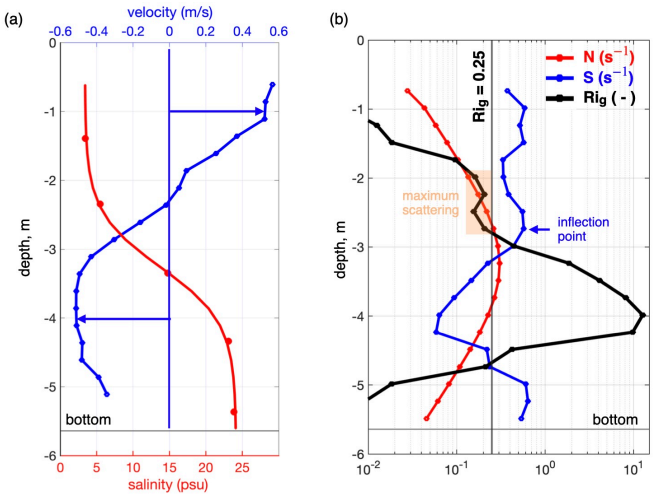

Figure 7. Typical profiles, here taken from transect T2. (a) Salinity (in red) at 75 m along-transect (see Figure 5). Note the five CTD sensors and the hyperbolic-tangent fit applied to all salinity data. The velocity profile from the ADCP was averaged over a 10 m horizontal window centered around distance 75 m. (70 − 80 m). (b) Buoyancy frequency N (red), shear S (blue) and $\mathrm{Ri_g}$ (black). Maximum scattering from mixing occurs in figure 5 occurs where $\mathrm{Ri_g} < 0.25$ and $N > 0.15\,\mathrm{s}^{-1}$ (highlighted in orange).

3 Conditions, forcing and energetics of the primary KH instability

3.1 Background conditions

Typical profiles from T2 mid-transect are shown in figure 7. We plot velocity and salinity (panel a), as well as N, S, and $\mathrm{Ri_g}$ (panel b). We find that the velocity profile exhibits a main inflection point within the pycnocline at 2.5–3 m depth, coinciding with a shear maximum, which are necessary conditions for shear instability (Smyth & Carpenter, 2019). At this depth, the velocity is approximately -0.1 to $-0.2\,\mathrm{m\,s}^{-1}$ (negative, i.e. landward), which also represents the expected propagation speed of KH instability. The gradient Richardson number $\mathrm{Ri_g}$ is likewise robustly below 0.25 here, confirming the possibility of KH instability, although it also drops below this threshold nearer the bottom and surface. As highlighted by the orange rectangle, the maximum scattering due to KH instability observed earlier in figure 5c occurs at the main inflection point corresponding to the pycnocline rather than in the near-bottom or near-surface layers. This is consistent with Eq. (4), since backscatter is a proxy for turbulent mixing (not just turbulence), and both salinity variance and its dissipation are orders of magnitude larger in the pycnocline (identified in this paper by $N > 0.15\,\mathrm{s}^{-1}$). Salinity ranges from ≈ 3 to 23 psu. Notably, the salinity and velocity inflection points are not colocated: the peak in N (corresponding to the mid-pycnocline salinity of 13 psu) is offset ≈ 0.5 m below the peak in S, making the KH instability slightly top-down asymmetric.

Figure 8(a) shows the joint probability distribution of N and S for all transects T1–T3 at depths of $2 - 4$ m, corresponding to the main pycnocline mixing zone. In the unstable region with maximum scattering (the orange triangle below the $\mathrm{Ri_g} = 0.25$ diagonal line), the typical range is $N \approx 0.15 - 0.3$ Hz and $S \approx 0.4 - 0.8$ Hz. A simple rule of thumb for the KH growth rate is $\approx S(1/4 - \min_z \mathrm{Ri_g})^{1/2} < S/2$ (Hazel, 1972), which here gives an upper bound of 0.4 Hz. These fast N and S timescales underscore why such shallow-wedge estuaries are well suited to the acoustic imaging of mixing: shallow depth and sharp salinity contrasts enhance the multibeam

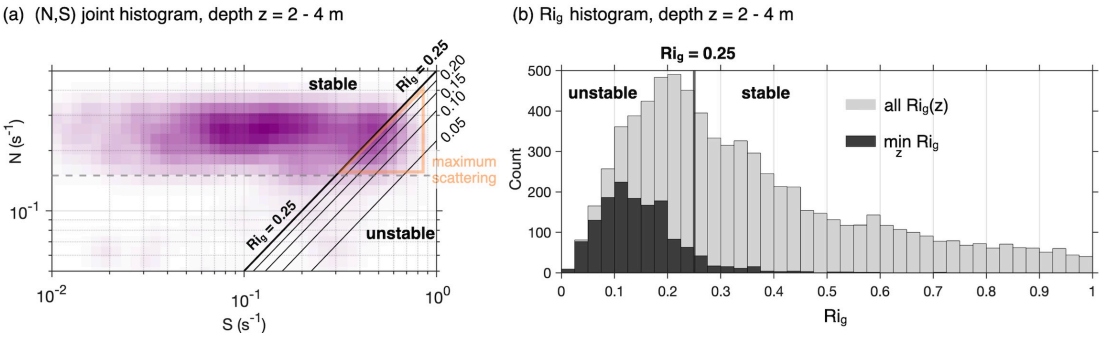

Figure 8. Typical N, S and $\mathrm{Ri_g}$ in all transects T1, T2, T3 between depths 2-4 m. (a) Joint histogram (S, N) with purple shading intensity proportional to probability density. The region of typical maximum scattering is highlighted. (b) Histogram of $\mathrm{Ri_g}$ (grey) with emphasis (black) on the distribution of the minimum $\mathrm{Ri_g}$ in each profile between $2-4$ m, showing a peak just below $\mathrm{Ri_g} = 0.15$, well below the marginal instability value of 0.25. The long tail of stable $\mathrm{Ri_g} > 1$ is not shown.

data resolution and signal-to-noise ratio, while intrinsic shear times of order one second allow instability trains to be tracked over just a few minutes.

Figure 8(b) shows the corresponding distribution of $\mathrm{Ri_g}$ (grey histogram), with particular emphasis on the minimum values across the 2-4 m depth range (black histogram). While the entire distribution peaks just below 0.25, consistent with prior measurements in this estuary (Geyer et al., 2017), the $\min_z \mathrm{Ri_g}$ distribution lies almost entirely below 0.25, is approximately normal, and peaks around $\mathrm{Ri_g} \approx 0.10 - 0.15$. This peak sits well below the linear stability threshold 0.25 (Eq 1), often cited in the literature on marginal instability as the value around which turbulence self-organizes, as found, for example, in the Pacific and Atlantic equatorial undercurrents (Smyth & Moum, 2013; Wenegrat & McPhaden, 2015; Smyth, 2020) and within internal solitary waves (M.-H. Chang, 2021). We interpret our submarginal $\mathrm{Ri_g}$ as evidence that turbulence in this estuary is strongly forced by the tide and the sloping pycnocline.

3.2 Large-scale baroclinic forcing and dissipation

This forcing can be modeled as follows. The primary (large-scale) slope of the pycnocline was estimated in transects T1–T3 to be $\alpha \approx 0.002$ (figures 4–6). Since the large-scale pressure gradient must remain nearly vertical (hydrostatic), the misaligned buoyancy gradient generates a baroclinic torque that energizes the shear at a rate

$$\frac{dS}{dt} \approx \alpha N^2, \tag{5}$$

where α denotes the (dimensionless) slope, noting that for small angles $\sin\alpha \approx \tan\alpha \approx \alpha \ll 1$. As a result, an initially stable water column with $\min_z \mathrm{Ri_g}(t=0) = \mathrm{Ri_{g0}} = N_0^2/S_0^2 > 0.25$ (say 0.3) will experience a steady decrease of this Richardson number following $\min_z \mathrm{Ri_g}(t) = \mathrm{Ri_{g0}}/(1 + 2\alpha\,\mathrm{Ri_{g0}}\,S_0 t)$. In other words, the timescale for halving the initial $\mathrm{Ri_g}$ from, say, 0.3 to 0.15 under this baroclinic tidal slope is $(2\alpha \mathrm{Ri_{g0}} S_0)^{-1}$; in our case $\approx (2 \times 0.002 \times 0.3 \times 0.3)^{-1} \approx 46$ min. This is much shorter than the tidal period, consistent with our argument that baroclinic forcing is the primary mechanism driving the flow to a state of submarginal instability within a single tidal phase. In our shallow estuary, baroclinic shear arises from the time-dependent response of the pycnocline to tidal forcing in the presence of bathymetric slopes. In transect T0, the primary slope of the pycnocline supporting the KH billow train matches the bathymetric slope $\alpha = 0.02$

(see figure 1a,c) – an order of magnitude steeper than in T1–3 and implies a forcing timescale for $\mathrm{Ri_g}$ about ten times faster, of order 5 min.

The baroclinically-forced decrease in $\mathrm{Ri_g}$ will eventually be arrested once turbulence becomes strong enough, at an equilibrium value $\mathrm{Ri_g} \approx 0.1$ – 0.15. This value must be sufficiently below 0.25 to generate strong enough Reynolds stresses $\overline{u'w'}$ and associated energy dissipation ϵ to balance the forcing αN^2 and establish a turbulent steady state for the shear:

$$\frac{\partial S}{\partial t} \approx \alpha N^2 - |\partial_{zz}\overline{u'w'}| \approx 0. \tag{6}$$

Solving for the Reynolds stresses across the shear layer $z \in [0, \delta]$, we find $\overline{u'w'} \approx \alpha N^2 z(z-\delta) \propto \alpha N^2 \delta^2$. The corresponding dissipation within the large-scale turbulent pycnocline largely follows the shear production (the buoyancy flux is small, since mixing efficiency is typically $\Gamma \ll 1$) and must therefore scale like

$$\epsilon \propto P = |\overline{u'w'}|S \propto \alpha\, N^2\, \Delta U\, \delta \propto \alpha\, \mathrm{Ri_g} \frac{(\Delta U)^3}{\delta}, \tag{7}$$

where $\Delta U = S\,\delta$ is the total velocity differential across the shear layer.

In Sec. 5.2, we return to this to quantify small-scale dissipation within the braids, which we will argue is likewise driven by baroclinic-slope forcing. The last equality in Eq. (7) includes a pre-factor of order 0.05, as we will show later in Eq. (14). Using this prefactor, we estimate the large-scale average just below $\epsilon \approx 10^{-5}\,\mathrm{m^2\,s^{-3}}$ (using $\Delta U = 1\,\mathrm{m\,s^{-1}}$, $\delta = 2\,\mathrm{m}$ from figure 7, and the typical $\alpha = 0.002$ from figures 4-6). This estimate is about three orders of magnitude above expected background levels in a quiescent estuarine pycnocline, and matches previous measurements in the same estuary (Lavery et al., 2013, figure 8a), lending support to the above forcing mechanism and energy balance. Yet these previous measurements also revealed rare and highly-localized peaks at $\epsilon \sim 10^{-3}\,\mathrm{m^2\,s^{-3}}$ (Lavery et al., 2013, figure 8a) and (Holleman et al., 2016, figure 7a), suggesting that the large-scale pycnocline average may conceal smaller, more intensely dissipative structures – the focus of this paper.

3.3 Turbulent lengthscales and multiscale approach

We end this section by outlining the expected hierarchy lengthscales in the turbulent cascade of our estuarine data.The challenge arises from the very high Reynolds number Re and Schmidt number Sc (defined as the ratio of ν to the molecular diffusivity of salt D). In transects T1-3, we find that

$$\mathrm{Re} = \frac{(\Delta U/2)(\delta/2)}{\nu} \approx 7.1 - 8.8 \times 10^5 \quad \text{and} \quad \mathrm{Sc} = \frac{\nu}{D} \approx 600 - 1000 \tag{8}$$

For Re we used the transect-averaged velocity profiles, half the total velocity differential ΔU and half the shear layer depth δ for consistency with much of the literature of stratified shear instabilities. We also used an averaged $\nu = 1.05 \times 10^{-6}\ \ \mathrm{m^2\,s^{-1}}$. For the range of Sc we used the salinity-dependent values of ν and D for sodium and chloride ions in the mixing range 5-20 psu, at the average temperature of 20 °C. To fix ideas, here and in the remainder of the paper, we shall use the following representative values

$$\mathrm{Ri_g} = 0.15, \qquad \mathrm{Re} = 8 \times 10^5, \qquad \mathrm{Sc} = 700. \tag{9}$$

We also recall our conservative large-scale estimate $\epsilon \sim 10^{-5} - 10^{-4}\,\mathrm{m^2\,s^{-3}}$, supported both by the baroclinic-slope forcing scaling and previous measurements in this estuary, and that maximum scattering (mixing) occurs at $N \sim 0.15 - 0.2 \sim 10^{-0.75}\,\mathrm{s^{-1}}$. Using these values, we

estimate the three key lengthscales – the Ozmidov scale L_O, the Kolmogorov scale L_K and the Batchelor scale L_B – as

$$L_O = \left(\frac{\epsilon}{N^3}\right)^{1/2} \approx 2\text{–}6\,\text{cm}, \quad L_K = \left(\frac{\nu^3}{\epsilon}\right)^{1/4} \approx 0.4\text{–}0.6\,\text{mm}, \quad L_B = \frac{L_K}{\text{Sc}^{1/2}} \approx 13\text{–}25\,\mu\text{m}. \tag{10}$$

The Ozmidov scale can be interpreted as the largest horizontal scale with sufficient kinetic energy to overturn (Riley & Lindborg, 2008). At scales smaller than L_O, we expect essentially unstratified, 3D turbulence, with a $k^{-5/3}$ inertial subrange in both the kinetic energy and scalar variance spectra, extending down to a few L_K. At scales below a few L_K, velocity fluctuations are exponentially damped, but scalar (salinity) fluctuations persist because of the high Sc. In this viscous–convective subrange the scalar variance spectrum likely follows a k^{-1} scaling down to a few L_B (Kundu et al., 2016, Chap. 12), where resolving structures typically remains beyond present observational, experimental and numerical capabilities at such high Sc.

The separation between L_O and L_K quantifies the width of the inertial range. Through the equality $L_O/L_K = \text{Re}_\text{b}^{3/4}$, it connects to the buoyancy Reynolds number Re_b, considered the key parameter of stratified turbulence, which we estimate as

$$\text{Re}_\text{b} = \frac{\epsilon}{\nu N^2} \approx 10^{2.5} - 10^{3.5} \approx 300 - 3000. \tag{11}$$

Prior studies argued that a dynamic range of $\text{Re}_\text{b} \gtrsim 30$ is necessary to the existence of an inertial range, and thus, of stratified turbulence (Bartello & Tobias, 2013), and that $\text{Re}_\text{b} \gtrsim 300$ is necessary to small-scale isotropy (Portwood et al., 2019). The above range of large-scale Re_b in the main pycnocline indicates strongly energetic stratified turbulence, and is consistent with prior data in this estuary (Holleman et al., 2016, figure 10), though they report higher peak Re_b presumably from using small-scale peak ϵ value. This range of Re_b was found in other strongly-stratified estuaries (Geyer et al., 2008), and more broadly, in other forced environments like mid-ocean ridges, the equatorial undercurrent, Arctic fjords, lake hypolimnia, the main thermocline, and the upper oceanic mixed layer (Jackson & Rehmann, 2014, figure 14). This similitude in Re_b underscores the broad relevance of our estuarine data for ocean mixing.

To bridge the hierarchy of turbulent mixing processes, we combine (i) ADCP/CTD data defining the large-scale hydrodynamic and energetic context at the meter scale, (ii) detailed acoustic observations resolving anisotropic braid structures down to cm scale, near the Ozmidov limit, and (iii) numerical simulations and laboratory experiments extending the picture to the sub-mm Kolmogorov scale.

4 Detailed acoustic observations

4.1 Multibeam visualizations of shear instabilities at peak amplitude

We now turn to instantaneous multibeam visualizations of the shear instabilities that mix the main pycnocline. Figure 9 presents 30 snapshots from transects T1–T3 at the locations labeled A, B, C, ... in figures 4–6c. The multibeam aperture, together with the shallow depth (1 – 5 m), provides an 8 m horizontal window, typically spanning a single instability wavelength. As the vessel progresses along the transect, individual instability 'events' between $2-4$ m depth enter and exit this window while evolving under their own dynamics, including: (i) growth, seen in the movies as steepening of the bright yellow high-χ_s structures; (ii) decay, as the structures flatten; (iii) own right-to-left propagation, caused by the typical landward velocity at the velocity inflection point; and (iv) highly-nonlinear distortion, including merging and splitting of wavelengths, and occasional interference with instabilities nearer the surface (examples of these temporal evolutions are shown in the next section). These 30 snapshots capture all distinct instability events in T1–T3 at peak amplitude (i.e. maximum slope).

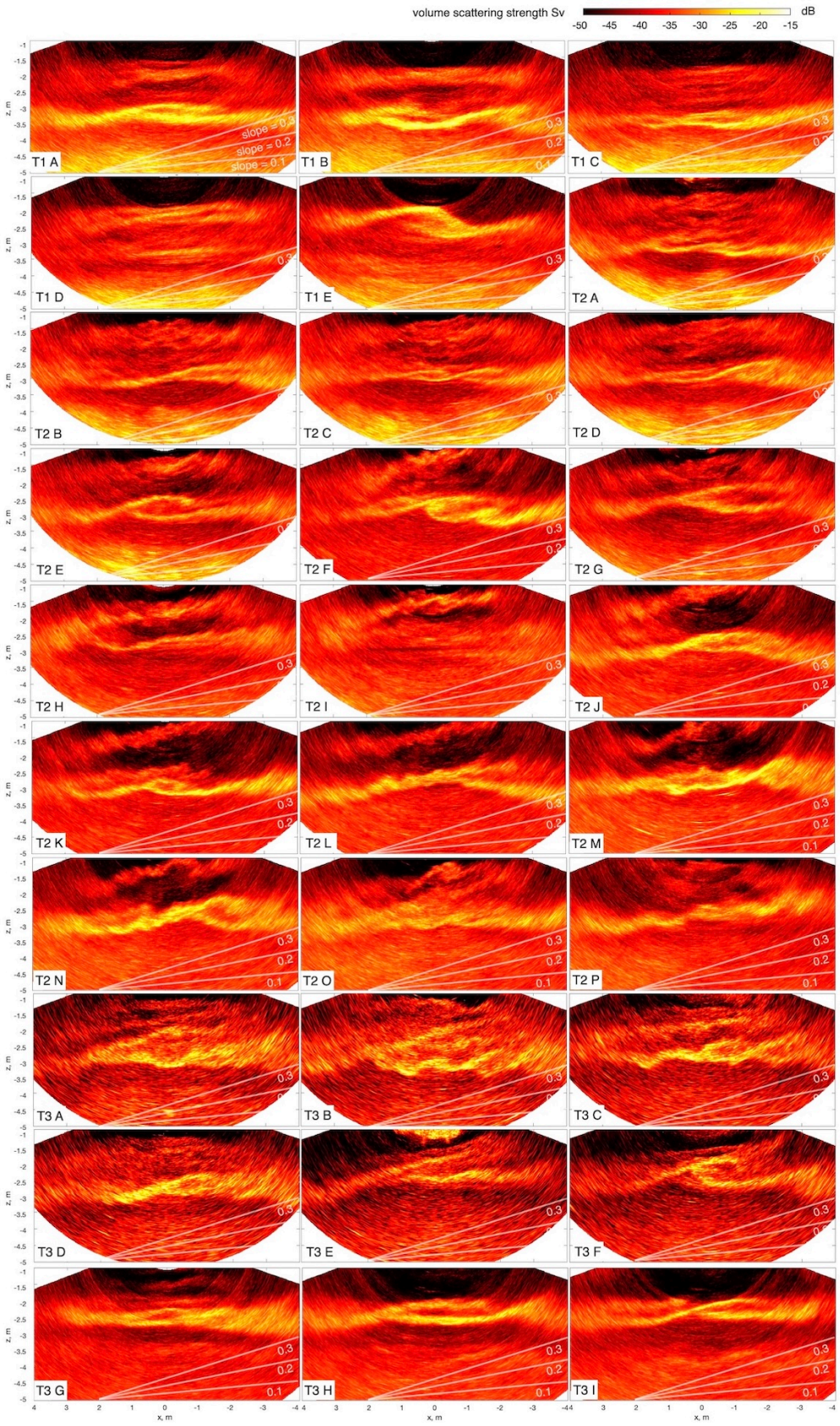

Figure 9. Multibeam imagery of shear instabilities in 30 separate events selected at maximum amplitude. Volume scattering strength S_V is proportional to mixing $\log_{10} \chi_s$ (Eq. 4). Snapshot lettering is as per figures 4-6c, e.g. 'T1 A' refers to transect 1 at location 'A', etc. Right is seaward, so flow in the bottom layer ($z \lesssim 3\,\mathrm{m}$) is always right to left (flood tide), and vice versa in the surface layer.

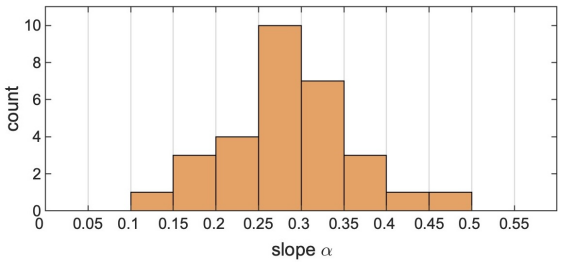

Figure 10. Histogram of braid slopes α estimated in the 30 representative multibeam snapshots in figure 9. The minimum and maximum observed values are 0.14 and 0.45, respectively.

Three important observations emerge from these visualizations. First, there is little, if any, evidence of 'bright cores', i.e. instabilities overturning at the scale of the primary KH billow (typically ∼1 m tall). Instead, intense turbulent mixing χ_s is concentrated along 'bright braids' and other thin, elongated structures between the primary 'quiet cores'. Single-beam observations had previously suggested this pattern in (Geyer et al., 2010) and in figure 1c, but for the first time multibeam imagery unequivocally confirms it and shows it is generic across a large sample of events spanning three transects.

Second, the bright turbulent braids exhibit shallow slopes, on the order of $\alpha \approx 0.1$–0.4 (see white guide lines in the bottom right of each panel). Figure 10 provides the histogram of slopes measured by fitting a line through the steepest, physically meaningful braid in each of the 30 snapshots. The distribution is approximately bell-shaped around the mean slope $\alpha \approx 0.25 - 0.35$. This observation is novel in that multibeam imagery provides true and reliable slopes, and it is significant in showing that, even at maximum amplitude, the instabilities do not steepen sufficiently (to, say, $\alpha \sim 1$) for billows to overturn and drive mixing directly. This stands in contrast to numerical simulations and laboratory experiments at comparable $\mathrm{Ri_g} = 0.1$–0.15 but lower $\mathrm{Re} \sim 10^3$–10^4 (see references in the introduction), where instabilities steepen further and cause the primary billow to overturn and mix.

Third, the bright braids occasionally display small-scale granularity, most clearly in panel T2E, suggesting discrete turbulent billow cores on the braid scale (∼10 cm). Later in this paper we argue that these features result from secondary KH instability on the braid itself. The relative rarity of such clear, discrete braid billows in figure 9 may be explained by two factors: (i) the acoustic data can only resolve structures larger than ∼5 cm, comparable to the braid billow height, so small individual billows may be smoothed into what appears as a continuous bright braid; (ii) this overturning billow stage may be inherently short-lived, followed by a much longer incoherent turbulent-braid phase, seen in most other snaphsots.

The added value of multibeam imagery compared with single-beam is illustrated in figure 11. We compare a selection of six of our multibeam snapshots (e.g. T1E, etc) with their corresponding synthetic middle-beam reconstructions (labeled T1E (R), etc). These reconstructions mimic what a single-beam echosounder, such as in the AUV data of figure 1, would record. These six examples differ in the time required for the vessel to sweep the 8 m window, depending on local vessel speed. Sweep time, noted above each panel, increases from left to right and top to bottom, making single-beam reconstructions progressively more prone to Doppler distortion as the instabilities evolve and move with finite phase speed while being scanned by the sonar. Faithful single-beam reconstructions would require sweep speeds much faster than the instability phase speed (here ~ 0.1–$0.2\,\mathrm{m\,s^{-1}}$), which is difficult to achieve in practice. Sweep direction, determined by the heading of the measurement platform, also matters: when the vessel moves with the

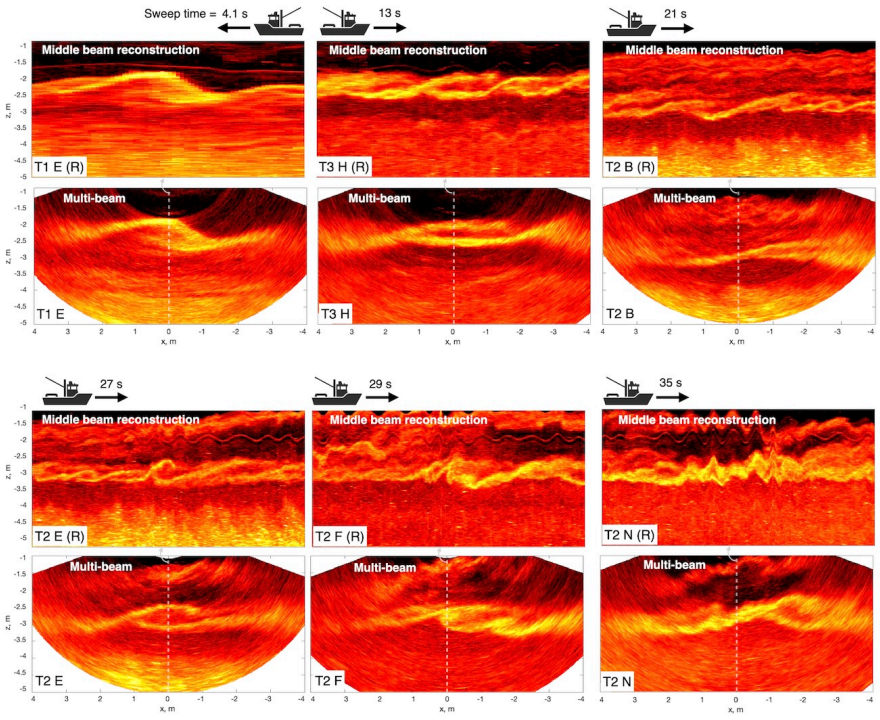

Figure 11. Multibeam imagery faithfully captures mixing structures, as demonstrated by contrast with middle-beam reconstructions, labelled (R), using the $x = 0$ beam. Multibeam snapshots are repeated from figure 9. Vessel sweep time increases from left to right and top to bottom, making single-beam imagery increasingly prone to distortion and thus unreliable to infer structures. Color range identical to figure 9.

instability (landward in T1), structures appear stretched and slopes flattened, whereas sweeps against the propagation direction (T2, T3) compress structures and steepen slopes. In both cases, distortion increases as sweep speed approaches wave speed. Accordingly, the most faithful single-beam reconstruction is found in T1E (top left), where the fast sweep speed $\approx 2\,\mathrm{m\,s^{-1}}$ and favorable direction yield the closest match to the multibeam. Single-beam images degrade progressively with slower sweep speeds and unfavorable vessel headings, becoming unrecognizable and misleading in T2F and T2N (sweep speeds ≈ 0.2–$0.3\,\mathrm{m\,s^{-1}}$). Thus KH wavelengths and aspect ratios inferred from single-beam acoustics in past studies (see e.g. (Tu et al., 2020, Table 1)) should be treated with caution.

4.2 Spatial evolution of the primary KH train

Using these insights, we reassess the single-beam T0 data from figure 1c, reproducing it in figure 12 enlarged with a true aspect ratio. Given the AUV's relatively fast sweep speed ($1\,\mathrm{m\,s^{-1}}$) and the favorable sweep direction (landward during flood tide), the structures in figure 12 are likely sufficiently faithful to provide supporting evidence to the multibeam observations from the previous section. We follow the spatial development of the primary instability over 73 m (panel a), with three 22 m sections enlarged in panels b–d, covering 11 separate wavelengths labeled #1-11 (average wavelength $\approx 5.5\,\mathrm{m}$). Note that the spatial evolution and wavelength number run from right to left and bottom to top.

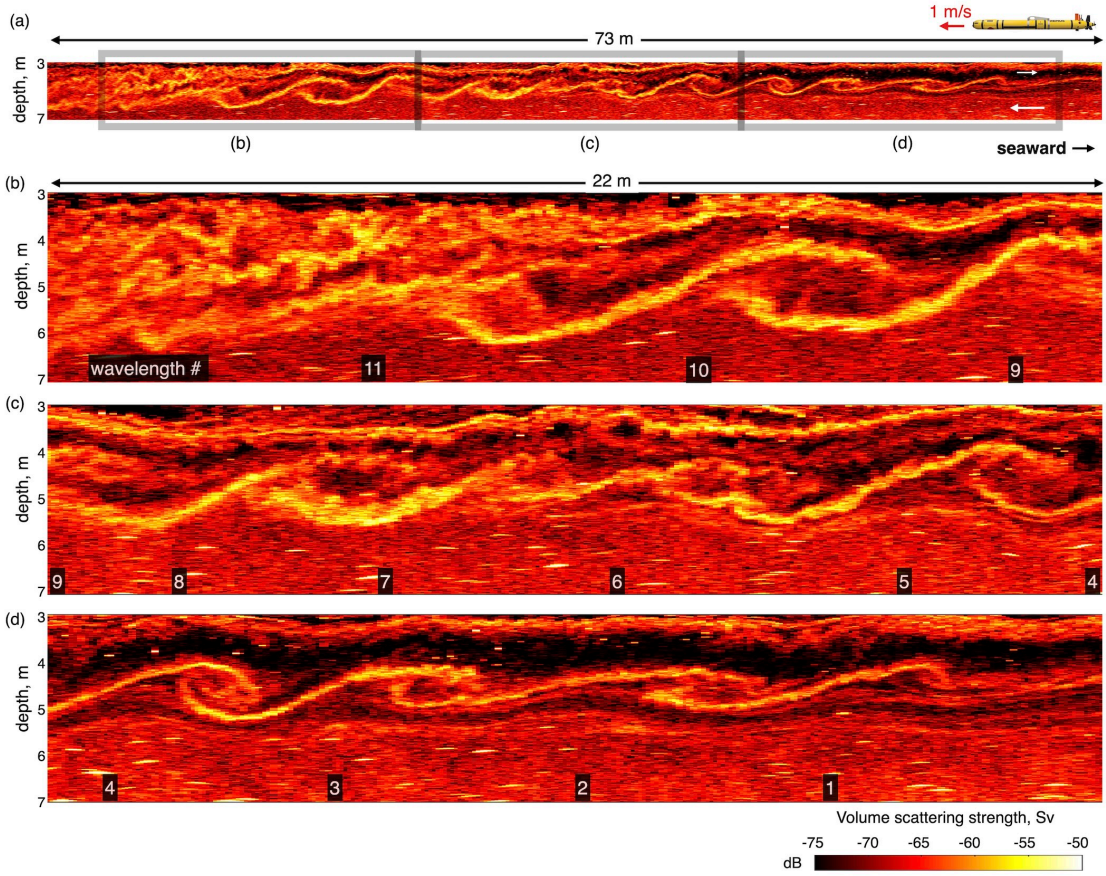

Figure 12. Zoom on the T0 data from figure 1, without vertical exaggeration (true aspect ratio), highlighting secondary instabilities within the braids. The long section from (a) is split into three 22 m-long enlarged sections in (b-d). Individual wavelengths are numbered 1-11 in chronological order (the AUV sweep direction is landward, right to left). As with any single-beam data, structures and slopes remain uncertain but are reasonably accurate here due to the fast sweep speed and favorable heading.

In the early stages of instability (# 1–2, panel d), we find thin braids (thickness ≈ 1-3 cm) and moderate slopes, gradually steepening in # 3–4. Notably, a partial overturn of a primary KH billow occurs between # 3–4 – a rare event, consistent with our earlier observations. Nevertheless, even in this case of partial overturn, mixing remains concentrated in the bright 'eyelids', extensions of the braid that wrap around the core or 'eye', rather than within the cores themselves, ruling out mixing caused by gravitational collapse of the 1 m-tall core.

At intermediate and later stages (# 4–10, panels c and b), braids continue to steepen without primary overturn. Some braids develop marked granularity, particularly evident in # 5, confirming the presence of secondary instabilities. The more mature braids (# 9–10) are thicker (≈ 10 cm) and slightly brighter, indicating that turbulence and mixing have intensified and spread across the braid, likely triggered by the earlier secondary instabilities and sustained by the baroclinic slopes of the braids.

At the later stages of the instability (# 11 and leftwards, panel b), further downstream of the mean landward flow, the braid loses coherence and breaks down into more disorganized

turbulence. This turbulence, however, remains roughly aligned with the former braid slope (and underlying isopycnals) and continues to sustain high levels of mixing.

4.3 Multibeam visualization of the lifecycle of mixing

We now seek to better understand the complex lifecycle of these instability structures, one wavelength at a time, by returning to time-resolved multibeam imagery. In figures 13-14 we show six sequences of snapshots from transects T2 and T3, with elapsed time indicated on the left. Each column follows an events in the vicinity of the snapshots shown earlier at maximum amplitude (e.g. T2D and T2E in figure 13a etc), now extended in time to reveal their growth and decay. Unlike previous visualizations, here the scattering strength is normalized by the transect-mean background ($|S_V(x,z,t|)/|\overline{S_V}(x,z)|$) to enhance contrast and highlight regions of elevated $\log_{10}\chi_s$ relative to the substantial background in this environment. Grey overlaid annotations indicate the slopes of the most meaningful braids and wavelength numbers # to track events as they propagate and distort across frames. Additional yellow annotations highlight key dynamical features identified after careful inspection of the 17 Hz movies, condensing a large amount of information.

The first sequence in figure 13a shows an initially steep braid ($\alpha = 0.44$ at $t = 0$) propagating leftward (landward) over several seconds, maintaining a nearly constant slope ($\alpha \approx 0.35$). Braid mixing initially peaks at the inflection point ($t = 1.29$ and 2.65 s), where the local straining field arises from deflection of the mean shear around the meter-tall billows on either side. A few seconds later ($t = 3.82$ and 4.41 s), mixing intensifies further downstream in a train of smaller-scale billows that grow spatially along the braid and into the eyelids, under advection on either side of the inflection point ($t = 5.12$ s). These small turbulent eyelid billows, with wavelength ≈ 0.4 m, eventually concentrate most of the mixing in the pycnocline. Less than a second later ($t = 5.82$ s), eyelid mixing weakens rapidly, leaving only 'fossil' mixing ($t = 7.35$ s). Throughout this event, the primary core remains dark, indicating no mixing above background levels and confirming that it does not overturn. This sequence reveals a timescale of about 5 s for sustained braid and eyelid turbulence, followed by decay over ≈ 2 s. Assuming similarity between primary and secondary KH instabilities, the observed secondary billow wavelength (≈ 0.4 m) implies a braid thickness $\delta_b \approx 10$–15 cm at the mature stage, consistent with our previous estimates.

The second sequence in figure 13b begins with a relatively weak braid # 1 ($\alpha = 0.23$) that steepens rapidly to $\alpha \approx 0.44$. Mixing is initially absent in the core, appearing instead in the braid and eyelid billows. Between $t = 1.94$ s and $t = 3.12$ s a large overturn develops through the roll-up of the bottom eyelid billows, yet the core remains dark, In the later frames ($t = 3.88$–5.52 s), the top eyelid experiences a similar fate, with roll-up to the right of the core, which remains shielded. The next braid # 2, coming from the right, starts steepening (from $\alpha = 0.23$ to 0.33), signalling the start of the next event. This sequence confirms that even strong steepening to $\alpha \approx 0.4$-0.5 does not trigger core mixing by large-scale gravitational collapse. Rather, turbulence grows and peaks in the braids and eyelids, and may occasionally be engulfed into the core – though this did not occur in the first sequence.

The third sequence in figure 13c features hows three successive wavelengths (# 1–3) propagating landward faster than in the previous sequences. All three follow a similar lifecycle to that described in figure 13a, giving robustness to our interpretation. A minor novelty appears at $t = 2.53$ s when a large eyelid billow from # 1 detaches, and is advected in the vicinity of the neighboring braid # 2 in subsequent frames ($t = 3.59$ – 4.76 s) before weakening ($t = 6.53$ s).

We now turn to figure 14 to illustrate some of the additional complexity in the lifecycles. The fourth sequence (figure 14a) begins with a fairly standard roll-up of braid billows into the

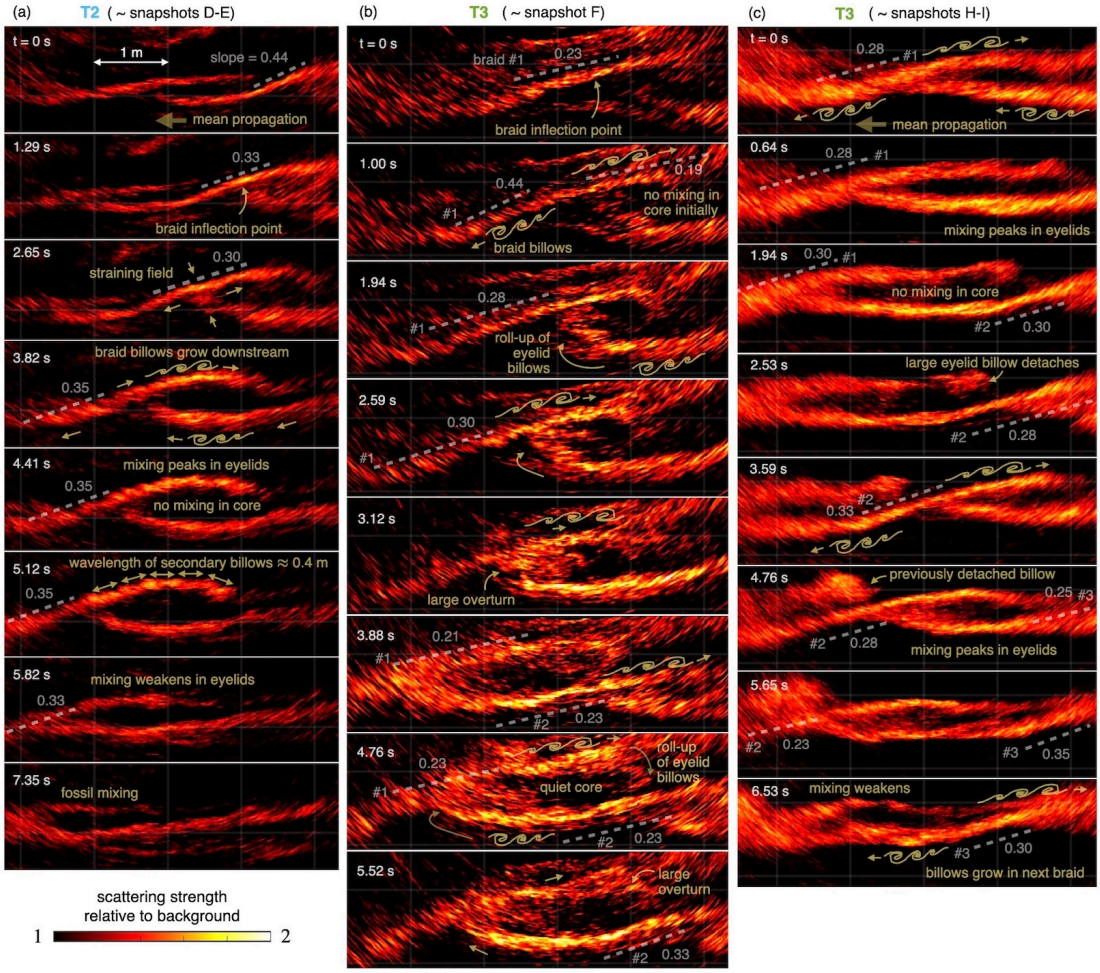

Figure 13. Temporal evolution of individual shear instabilities revealed by three multibeam sequences from T2 and T3 to illustrate their typical lifecycle. Each column shows one or two events around the maximum-amplitude snapshots from figure 9, extended in time to capture growth, overturn, and decay. Time increases downwards. Grey annotations helps track braid numbers # across frames and quantifies slopes. Yellow annotations condense dynamical information from the movies. The scattering strength is normalized by the transect-mean background. The light-grey grid has 1 m spacing.

core. From $t = 3.41$ s, however, braid #3 steepens dramatically and then stretches and splits ($t = 6.87$ s), likely under intense strain. The splitting generates braid #4, which then follows the more typical lifecycle.

The fifth sequence (figure 14b) begins with the familiar pattern of fossilizing eyelids, but gradually transforms into what appears to be a Holmboe instability ($t = 0 - 4.71$ s), recognizable by the characteristic cusps (Carpenter et al., 2010) in the turbulent pycnocline. The Holmboe instability is a strongly-stratified cousin of the KH instability found when the pycnocline is much thinner than the surrounding shear layer (Caulfield, 1994). Here, it could be a local, temporary flow state after the mean shear has been weakened by a turbulent event and before it is re-energized by the baroclinic-slope forcing. Soon after, this pycnocline ($t = 6.47$ s) steepens again ($t = 8.88$ s) as the primary KH instability redevelops following the typical lifecycle.

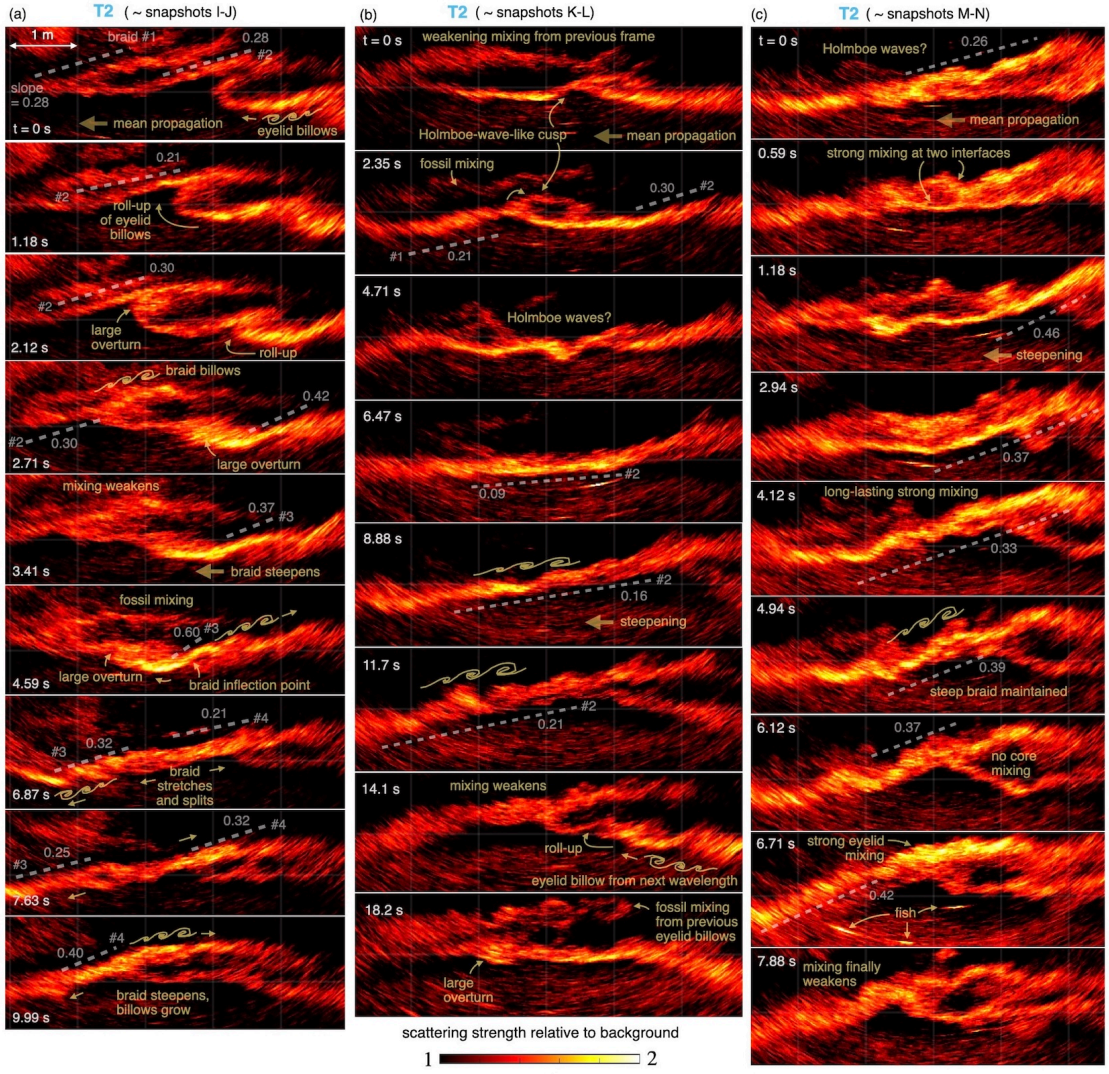

Figure 14. Temporal evolution of individual shear instabilities shown in three further multibeam sequences from T2 to illustrate more complex dynamics. Legend as in figure 13.

The sixth and last sequence (figure 14c) starts with Holmboe-like cusps revealing strong mixing at two interfaces ($t = 0.59$–$2.94\,\mathrm{s}$), with a braid that transiently steepens to a rarely seen $\alpha = 0.46$. It then flattens to more typical $\alpha = 0.3$–0.4 and sustains intense mixing for a typical $\approx 5\,\mathrm{s}$, with signs of stretching and splitting, while the core remains dark throughout. Eyelid mixing peaks and thickens ($t = 6.71\,\mathrm{s}$) before suddenly weakening ($t = 7.88\,\mathrm{s}$).

The observations in this section show that, in the continuously forced regime, the lifecycle of shear instabilities only lasts a few shear timescales, which is at least an order of magnitude faster than that of the idealised KH instabilities typically simulated. These observations also raise at least three questions that we turn to next with modeling. Why do braids consistently develop secondary small-scale billows where mixing concentrates, and what are the relevant local length- and timescales? How is turbulence in the braids and eyelids generated and sustained, and what levels of ϵ and χ_s should we expect at the braid (Ozmidov) scale of $\sim 10\,\mathrm{cm}$? How does mixing look like well below the braid scale, down to the Kolmogorov scale?

5 Modeling and discussion

5.1 Secondary KH instabilities predicted from numerical simulations

To understand why secondary billows consistently appear along the braids while cores remain quiet, we conducted 2D direct numerical simulations (DNS) at representative field conditions. The flow was initialized with hyperbolic-tangent velocity and salinity profiles consistent with the typical profiles in figure 7, with dimensionless parameters set to our representative field values $(\mathrm{Ri_g}, \mathrm{Re}, \mathrm{Sc}) = (0.15, 8 \times 10^5, 700)$ (see Eq. 9). The Navier–Stokes equations under the Boussinesq approximation were solved with `Oceananigans.jl` (Ramadhan et al., 2020) with very fine resolution ($10^4 \times 10^4$ grid points) to capture braid sharpening. Details of the numerical setup (grid, initial and boundary conditions) are given in Appendix B.

Figure 15(a–f) illustrates the evolution of the primary KH braid. At $t = 30\,\mathrm{s}$ it has slope $\alpha \approx 0.2$ (panels a-b); by $t = 45\,\mathrm{s}$ it steepens to $\alpha \approx 0.3$ and shows signs of instability (panels c-d), and by $t = 50\,\mathrm{s}$ it has developed secondary KH billows at $\alpha \approx 0.4$ (panels e-f). The dynamics are expected to remain essentially 2D until soon after $t = 45\,\mathrm{s}$. By $t = 50\,\mathrm{s}$, the secondary billows have already overturned multiple times (see zoom in panel g), implying that in three dimensions they would have already transitioned to turbulence, before the primary billows themselves overturn significantly. Thus, these simulations confirm that, at these field-matched parameters, vigorous turbulence on the braid is expected to precede primary core turbulence.

The simulation agree closely with the observations on three points, strengthening our confidence in their relevance. First, the secondary billow spacing ($\sim 40\,\mathrm{cm}$) and height ($\sim 10\,\mathrm{cm}$) shown in panel g match the multibeam imagery. Once turbulent, the braid may thicken slightly by entrainment, consistent with our earlier estimate $\delta_b \approx 10$–$15\,\mathrm{cm}$ at the mature stage. Second, simulated braid slopes (panels b,d,e) fall in the observed range $\alpha = 0.2$–0.4 (figure 10) and confirm that braid turbulence sets in around $\alpha \approx 0.4$. Steeper slopes, which would favor primary overturn, are rare in the field presumably because braid turbulence and dissipation intervene first and arrest primary growth. Third, the simulated mixing structure ($\log_{10} \chi_s$) is consistent with the multibeam echosounder signal. To illustrate this, panel (h) shows a synthetic backscatter obtained by Gaussian smoothing and colormap clipping below $\chi_s < 10^{-4.5}\,\mathrm{psu^2\,s^{-1}}$, mimicking sonar acquisition and emphasizing only mixing above pycnocline background levels. The result strongly resembles figure 13(a) around peak mixing ($t = 4.41\,\mathrm{s}$).

What mechanism drives this secondary instability? As the braid steepens, it experiences a compressive strain field from the deflection of the mean flow around the growing billows (see velocity vectors in panel g) (Corcos & Sherman, 1976). This strain $\gamma = |\partial w/\partial z|$ is initially sufficient to stabilize the braid (Corcos & Sherman, 1976; Dritschel et al., 1991; Staquet, 1995; Smyth, 2003). As the braid slope α increases, baroclinic forcing amplifies the shear at a rate $dS/dt \approx \alpha N^2$ (recall Eq. 5), while strain compresses the isopycnals and increases N^2, sharpening both the pycnocline and the shear layer, as seen in the vertical profiles in panel (i). At high Re and Sc, diffusivities are too small to smooth these gradients, allowing local shear to intensify much more rapidly than strain, whose growth remains moderate and controlled by the large-scale primary billow. Previous studies suggest that once S/γ exceeds a threshold (Staquet, 1995; Smyth, 2003; Mashayek & Peltier, 2012a), the braid succumbs to secondary KH instability. When the secondary billows saturate – here around $t = 50\,\mathrm{s}$ – the effective braid thickness (secondary billow height) is $\sim 10\,\mathrm{cm}$, but the velocity and salinity profiles are no longer hyperbolic–tangent, i.e. similar to the larger scale. A fine zoom on the braid (panel j) shows that, within it, even from $t = 45\,\mathrm{s}$, the sharpest gradients are confined to an even thinner $\sim 2\,\mathrm{cm}$ interface (dashed box). This intense local sharpening is consistent with prior high-resolution CTD measurements in this estuary revealing $\sim 1\,\mathrm{cm}$-sharp pycnoclines (figure 6b in (Holleman et al., 2016)). Within

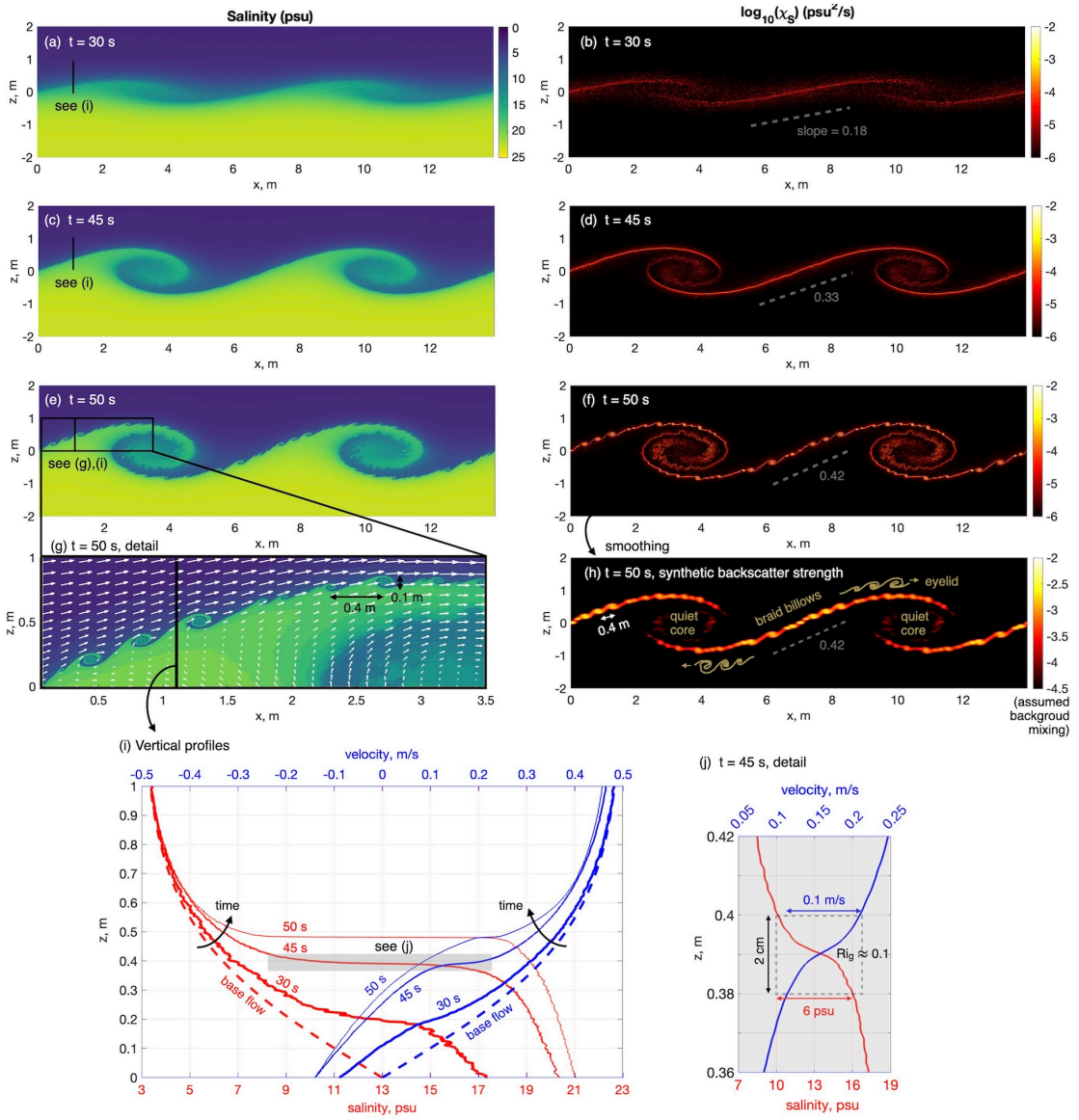

Figure 15. Two-dimensional direct numerical simulation revealing secondary KH instability on the braid at field-matched $(\mathrm{Ri_g}, \mathrm{Re}, \mathrm{Sc})$. (a,c,e) Salinity and (b,d,f) its mixing rate $\log_{10}\chi_s$ at $t = 30, 45, 50\,\mathrm{s}$ after initialization. (g) Zoom on the salinity with velocity vectors, showing the braid after onset of secondary instability. (h) Synthetic backscatter obtained by Gaussian smoothing and colormap clipping so that values below the expected background $\chi_s < 10^{-4.5}\,\mathrm{psu}^2\,\mathrm{s}^{-1}$ appear as baseline (black) for comparison with figures 13-14. Two wavelengths are shown for clarity, and the domain has been cropped to $z \in [-2, 2]\,\mathrm{m}$. (i) Vertical profiles across the braid, showing extreme sharpening over time. (j) Detail over a 6-cm window within the braid at onset of secondary instability.

the 2 cm interface in figure 15(j), $\mathrm{Ri_g} \approx 0.1$ and the local shear is amplified five-fold relative to the initial primary shear, making the secondary KH instability both more weakly stratified than its parent and faster in timescale.

These findings support the view, developed in earlier work (Klaassen & Peltier, 1985, 1989, 1991; Caulfield & Peltier, 2000; Mashayek & Peltier, 2012a, 2012b), that the emergence of

higher-order instabilities is primarily controlled by Reynolds number. With the parameters of this simulation, however, tertiary instabilities are not observed at cm scale. Although by $t = 50\,\mathrm{s}$ the secondary braids between the secondary billows have sharpened by another order of magnitude to 2 mm (not shown, but still comfortably resolved by our stretched grid), the primary braid scale Reynolds number remains only $\mathrm{Re} \sim 5000$, too low for shear to overcome strain and sustain another instability cycle. We conclude that triggering tertiary instabilities before secondary billow overturn and turbulence would require sharper secondary braids made possible by a higher large-scale $\mathrm{Re} > 10^6$ typical of deeper environments (see Appendix A).

5.2 Braid turbulence energetics and visualization from laboratory experiments

What happens after the transition to 3D turbulence? Our multibeam observations showed that mixing is typically sustained for periods of $\approx 5\,\mathrm{s}$, corresponding to $\approx 10 - 20$ braid shear timescales (figures 13-14). To probe this regime, we now combine observations, simulations, and laboratory experiments, as sketched in figure 16. Braid turbulence persists when local baroclinic production balances turbulent dissipation, the same mechanism invoked at the estuarine scale in Eq. 6. This balance rests on three assumptions: (i) approximate homogeneity along the braid (valid away from curvature and eyelids; see figure 16a); (ii) approximate stationarity (valid during periods of nearly constant slope and turbulence intensity, observed in the multibeam sequences); and (iii) negligible strain compared to shear (a prerequisite for secondary instability, see figure 16b). This continuously forced turbulent state has been reproduced in the stratified inclined duct (SID) laboratory experiment (see figure 16c). The SID drives a pure baroclinic exchange flow through a long, sloping duct connecting two reservoirs of different salinity (Meyer & Linden, 2014; Lefauve & Linden, 2020), conceptually similar to Thorpe's classic tilted-tube experiments (Thorpe, 1971) but sustained for hundreds of shear times.

The SID experiment enables detailed, non-intrusive optical measurements of turbulence energetics, with time-resolved, 3D velocity and salinity fields resolved down to the Kolmogorov scale using simultaneous stereo particle image velocimetry and laser-induced fluorescence (Partridge et al., 2019). As reviewed in (Lefauve, 2024), these measurements show that the turbulence within the duct interior also satisfies Eq. (6) under the same assumptions, making it a faithful laboratory analogue for braid turbulence. This analogy is illustrated in figure 16(d–e) by comparing the braid-scale salinity and velocity from simulation at the onset of secondary instability (panel d) with those from the laboratory during sustained turbulence (panel e), both shown in the local frame sloping at angle α. The cyan boxes highlight the shear layer (braid) thickness δ where the analogy holds. A few braid shear times after the onset of secondary KH instability (panel d), this region is expected to transition to 3D turbulence and enter the SID-like regime away from boundaries (panel e). This equilibrium corresponds to the mature braid, where dissipation ϵ and mixing χ_s peak, as in the brightest signal in the multibeam sequences.

The turbulent kinetic energy dissipation in the braid was confirmed by SID data and supporting modeling (Lefauve & Linden, 2022b, Sec. 3) (Zhu et al., 2023, Sec. 5.4) to be

$$\epsilon \approx \frac{1}{16}\,\alpha\,\mathrm{Ri_g}\,(1-\Gamma)\,\frac{(\Delta U)^3}{\delta}. \tag{12}$$

Eq. (12) is adapted from (Lefauve, 2024, Eq. (6)) but is written here in physical units. Across the braid, the gradient Richardson number is expected to be $\mathrm{Ri_g} \approx 0.1 - 15$, matching the turbulent equilibrium found in SID experiments (Lefauve & Linden, 2022a), confirmed by DNS of SID (Zhu et al., 2023), and by higher-$\mathrm{Re_b}$ DNS in a similar shear-forced regime (Portwood et al., 2019). This range of $\mathrm{Ri_g}$ is also consistent with the peak in the pycnocline-scale histogram of $\min_z \mathrm{Ri_g}$ (figure 8b), where even at larger scales, continuous shear forcing sustains $\mathrm{Ri_g}$ well below marginal instability. The mixing efficiency $\Gamma = B/\epsilon \approx \chi/\epsilon$ – the ratio between buoyancy flux B

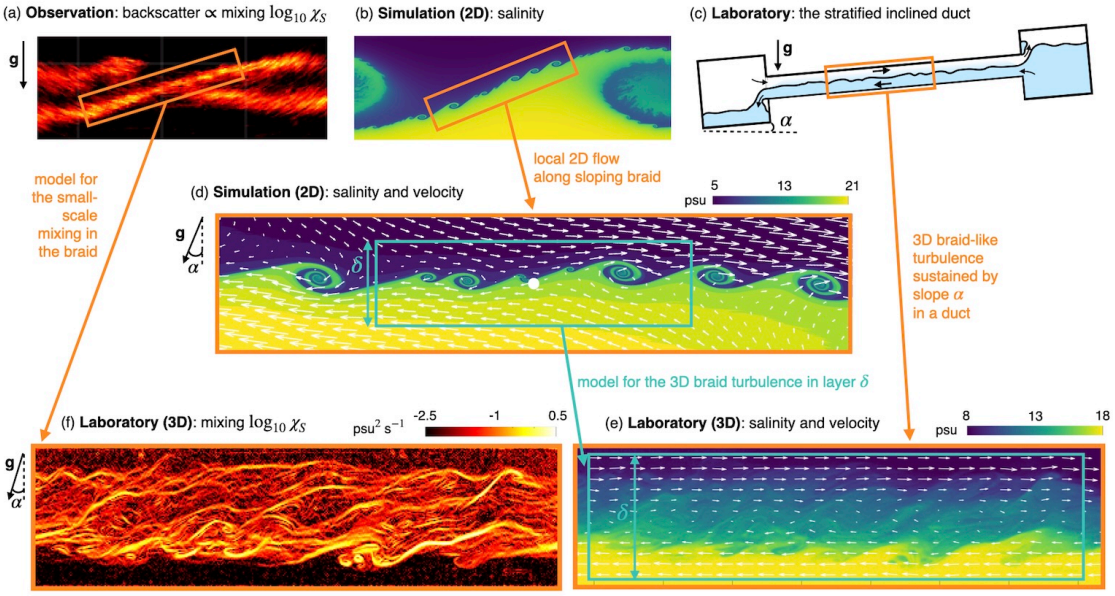

Figure 16. Bridging the gap to the smallest mixing scales by combining insights from (a) multibeam echosounder observations, (b,d) 2D direct numerical simulations, and (c,e,f) laboratory experiments. The stratified inclined duct (SID) setup (c) produces high-resolution salinity and velocity data (e, velocity vectors subsampled) in baroclinically forced stratified turbulence characteristic of the braid after the onset of secondary instability (d). SID data yield χ_s snapshots (f, here shown at the same instant as e), which serve as a model for braid mixing below the resolution of the observations in (a). In this experiment the duct height was 0.045 m, giving an effective shear layer – or 'braid' – with $\delta = 0.04\,\mathrm{m}$ (see cyan box in e); $\Delta U = 0.12\,\mathrm{m\,s^{-1}}$; and $\alpha = 0.1$, resulting in a local $\mathrm{Re} \approx 1200$ and $\mathrm{Re_b} \approx 25$, i.e. at the lower end of real braids. For further details, see main text and (Lefauve, 2024, figure 7).

(approximately mixing χ) and ϵ – is tightly linked to $\mathrm{Ri_g}$ through the turbulent Prandtl number $\mathrm{Pr_T}$, defined as the ratio of the turbulent diffusivity for density K_ρ and the eddy viscosity ν_T

$$\mathrm{Pr_T} = \frac{K_\rho}{\nu_T} = \frac{P/S^2}{B/N^2} = \frac{\Gamma\,\mathrm{Ri_g^{-1}}}{1+\Gamma} \qquad \text{hence} \qquad \Gamma = \frac{\mathrm{Ri_g}}{\mathrm{Pr_T} - \mathrm{Ri_g}} \approx 0.11 - 0.18, \tag{13}$$

using the expected range $\mathrm{Ri_g} \approx 0.1 - 15$ and $\mathrm{Pr_T} \approx 1$. A turbulent Prandtl number close to unity is supported both by measurements in the Connecticut River estuary (Holleman et al., 2016) and high-$\mathrm{Re_b}$, shear-forced DNS (Portwood et al., 2019), which showed that the turbulent processes that mix salt and and momentum in this regime are highly coupled and not substantially affected by the stratification. Assuming a braid-average $\Gamma \approx 0.15$, we can now estimate dissipation and mixing at the braid scale as

$$\epsilon \approx 0.05\,\alpha\,\mathrm{Ri_g}\,\frac{(\Delta U)^3}{\delta} \approx 7.5\times10^{-3}\,\alpha\,\frac{(\Delta U)^3}{\delta} \approx 2\times10^{-5} - 4\times10^{-4}\,\mathrm{m^2\,s^{-3}}, \tag{14}$$

$$\chi_s \approx (g\beta)^{-2}\,\Gamma\epsilon \approx\ 2.8\times10^{3}\epsilon \approx 2.1\,\alpha\,\frac{(\Delta U)^3}{\delta} \approx 5\times10^{-2} - 1\,\mathrm{psu^2\,s^{-1}}, \tag{15}$$

where all quantities are in the standard units (m, s and psu). Note that Eq. (14) provides the correct pre-factor (0.05) to our earlier scaling Eq. (7). To estimate the range in ϵ and χ_s we used for the braid thickness $\delta = 0.1$–$0.15\,\mathrm{m}$, and for the velocity differential $\Delta U = S\delta \approx 0.1$–$0.6\,\mathrm{m\,s^{-1}}$, based on the secondary braid shear being three to five times larger than the primary shear, i.e.

$S \approx 1$–$4\,\mathrm{Hz}$. This braid dissipation range is, as expected, higher than the pycnocline average level (just below $\epsilon \approx 10^{-5}\,\mathrm{m^2\,s^{-3}}$, see Sec. 3.2) and compares well with the peak levels measured in-situ (Lavery et al., 2013, figure 8a) (Holleman et al., 2016, figure 7a). This braid mixing range is also three to five orders of magnitude above typical estuarine background level, which, recalling Eq. (4), is consistent with the enhanced scattering strength range observed in our data.

Does the braid-elevated ϵ imply a higher buoyancy braid-scale Reynolds number $\mathrm{Re_b}$ compared to its large-scale counterpart? Noting the direct relation between $\mathrm{Re_b}$ and Re (the latter being based on half the velocity differential and layer thickness)

$$\mathrm{Re_b} = \frac{\epsilon}{\nu N^2} \approx 0.05\,\alpha\,\frac{\Delta U\,\delta}{\nu} \approx 0.2\,\alpha\,\mathrm{Re}, \tag{16}$$

we infer at the braid scale the range

$$\mathrm{Re_b} \approx 25 - 1800. \tag{17}$$

The lower values correspond to the thinnest, shallowest braids (e.g. wavelengths # 1-2 in figure 12) and the upper values to the thickest, steepest braids (e.g. wavelengths # 8-10 in figure 12). Eq. (16) is general and holds both at the braid scale, where $\alpha = 0.2$–0.4 and $\mathrm{Re} = 2500$–$22,500$ yield Eq. (17), and at the large pycnocline scale, where $\alpha = 0.002$–0.02 and $\mathrm{Re} = 8 \times 10^5$ yielded $\mathrm{Re_b} \approx 300$–$3000$ (Eq. 11). Thus, despite the higher ϵ, the braid $\mathrm{Re_b}$ remains comparable to – or even lower than – its large-scale counterpart, because N^2 also increases through the enhanced S^2 and $\mathrm{Ri_g} \approx 0.1 - 0.15$ remains constant across scales.

We conclude this section with the final key question of the paper: what does mixing look like at scales far below the resolution of field measurements, down to the Kolmogorov scale? Specifically, do we find evidence of secondary KH billows overturning within the lower-Re braid – i.e. small 'bright cores' – as would be inferred from the unforced case? Laboratory data provide the answer, resolving χ_s down to $< 0.1\,\mathrm{mm}$ in figure 16(f). (See also (Lefauve, 2024, figure 7) for corresponding snapshots of other flow variables including ϵ.) The dominant structures are long and thin filaments reminiscent of stacked braids but at much smaller scales (thickness $< \delta/25$). Crucially, these high-χ_s filaments remain relatively flat and statically stable, without evidence of elevated χ_s in overturning billows. In this experiment (see α, ΔU, and δ values in the caption), Eq. (15) predicts a braid-averaged $\chi_s \approx 10^{-2}\,\mathrm{psu^2\,s^{-1}}$ (dark red shades). Yet we find that the peak values within filaments exceed $\chi_s \approx 1\,\mathrm{psu^2\,s^{-1}}$ (yellow–white shades), two orders of magnitude above the mean, which would correspond to small-scale peaks of $\chi_s \approx 5 - 100\,\mathrm{psu^2\,s^{-1}}$ in the field. These values exceed existing measurements, likely because current instruments cannot resolve the small spatial and temporal scales over which such extremes occur. Such extreme concentration of χ at high Sc is consistent with emerging evidence from DNS (Petropoulos et al., 2024), though these DNS were limited to $\mathrm{Sc} = 7$ (thermally stratified water) and did not include mean shear.

Thus the structures shown in figure 16f are a valuable laboratory analogue for the expected structure well below the resolution of the acoustics in figure 16a. However, the exact scale separation between the braid thickness δ and the finer filaments is likely controlled by the braid $\mathrm{Re_b}$. This experiment has $\mathrm{Re_b} \approx 25$, matching the lowest braid-scale value expected in the field (recall Eq. 17). In this sense, the scale separation seen here is a lower bound of what occurs in reality, where thicker and steeper braids would generate even thinner and more extreme χ_s filaments. Our key conclusion, however, remains robust – when sustained by baroclinic forcing over many shear timescales, braid mixing is not dominated by secondary overturning billow cores but by thinner and stable filaments.

6 Conclusions

This paper proposes a new model for the energy cascade in ocean mixing hotspots, focusing on large-scale shear instabilities with continuous baroclinic forcing. A key novelty was the use of multibeam acoustic backscatter to reveal the true spatial structure and temporal evolution of mixing within trains of KH instabilities in the shallow Connecticut River estuary, an ideal natural laboratory. We sampled dozens of events across four transects, combining shipboard multibeam survey and co-located ADCP/CTD profiles with a more conventional single-beam survey from an AUV (Sec. 2). Although developed from estuarine observations with site-specific values, our predictive model is expressed in terms of local slopes, shear, velocity, and length scales, and thus generalizes to other mixing hotspots (Appendix A).

The large-scale hydrodynamic conditions in Sec. 3 show that the pycnocline in this estuary is primed for KH instability, with minimum $\mathrm{Ri_g}$ in the water column spanning 0–0.3 and peaking just below 0.15. Baroclinic forcing from tidal and bathymetric slopes steadily reduces $\mathrm{Ri_g}$ and sustains submarginal instability well below the threshold of $\mathrm{Ri_g} = 0.25$, which remains a powerful predictor for the occurrence of mixing in the acoustics. This equilibrium is explained by a balance between baroclinic shear production and turbulent dissipation (Eq. 6) and yields pycnocline-averaged dissipation $\epsilon \sim 10^{-5} - 10^{-4}\,\mathrm{m^2\,s^{-3}}$ (Eq. 7), in line with earlier measurements. Yet prior observations also revealed rare, localized peaks suggesting that large-scale averages conceal more intense, small-scale structures, motivating our subsequent focus on braids. The representative parameters at the estuarine scale ($\mathrm{Ri_g} = 0.15$, $\mathrm{Re} = 8 \times 10^5$, $\mathrm{Sc} \approx 700$) imply a turbulent cascade spanning from the meter scale to tens of microns (Eq. 10) – a high dynamic range controlled by $\mathrm{Re_b} \approx 300$–$3000$ (Eq. 11). These values confirm that the flow sits firmly in the regime of intense stratified turbulence, with broad relevance to mixing hotspots far beyond this single estuary.

The smaller-scale multibeam observations in Sec. 4 provide the first unambiguous view of the spatial structure and lifecycle of mixing within KH billow trains, confirming and refining arguments from (Geyer et al., 2010). Intense mixing is not generated by primary core overturn at the meter scale, as in lower-Re studies, but is instead concentrated along thin ($\approx 5 - 15\,\mathrm{cm}$) sloping braids with moderate slopes $\alpha \approx 0.2$–0.4 which extend into flatter eyelids. These braids steepen, spawn secondary billows, and grow thicker by intense turbulence, which is sustained and advected along the eyelids before decaying, typically over only $\approx 5\,\mathrm{s}$ (a few shear time scales) – an order of magnitude faster than the lifecycle of idealized, lower-Re KH billows. At times, eyelid turbulence detaches and interacts with neighboring wavelengths or rolls up into the primary core, highlighting the diversity of short-lived processes. Yet across many events, the consistent picture of braid-generated, eyelid-advected turbulence establishes it as the dominant high-Re mixing process. We emphasize that multibeam imagery was critical to reaching this conclusion, since single-beam systems used in past studies conflate space and time through the relative motion of the platform and the instabilities, obscuring both slopes (billow aspect ratio) and evolution.

The modeling in Sec. 5 explains why mixing originates in braids and how the cascade proceeds below observational resolution. Our 2D DNS in Sec. 5.1 at field-matched $(\mathrm{Ri_g}, \mathrm{Re}, \mathrm{Sc})$ shows that as braids steepen, baroclinic forcing of shear (Eq. 5) and strain-induced compression sharpen the pycnocline until shear dominates and secondary KH appears at the braid scale ($\delta_b \approx 10$ cm). The secondary KH mechanism is established in the literature, but our highly-resolved DNS provides a direct demonstration of its rapid onset and relevance at field parameters. Secondary KH instability pre-empts primary KH core overturn and shortcuts the transition to 3D turbulence because it evolves on faster timescales, due the amplification of braid shear. Tertiary KH instability does not generically arise at our estuarine $\mathrm{Re} \sim 10^6$ due to insufficient sharpening of the braids between secondary billows, but it is expected at higher Re.

The analysis of the ensuing braid turbulence regime in Sec. 5.2 completes this picture. After the fast 3D collapse of secondary billows, a turbulent braid with local Re $\sim 10^3 - 10^4$ persists for many local shear times in baroclinic-production–dissipation balance (Eq. 6). This balance mirrors that of the main pycnocline at smaller scale and steeper slope, and predicts braid dissipation ϵ (Eqs. 14) and mixing χ_s (Eq. 15) consistent with the bright braids observed in the acoustics and with the elevated in-situ values of prior studies. Despite the braids and eyelids exhibiting ϵ several times above the large-scale mean, their dynamic range $\mathrm{Re_b} \approx 25 - 1800$ (Eqs. 16 and 17) remains lower than the large-scale value because N^2 increases with S^2 at roughly constant $\mathrm{Ri_g} \approx 0.1 - 0.15$ across scales. The enhanced ϵ is thought to arrest the primary KH growth beyond $\alpha \approx 0.4$ and thus prevent overturn, but this conjecture is left for future work.

The baroclinic-production–dissipation balance is also reproduced in the stratified inclined duct (SID) experiment – a sustained downslope baroclinic exchange flow – at braid-matched $\mathrm{Ri_g}$, Re, and Sc. High-resolution optical measurements in SID extend our view of the cascade below the braid scale, resolving sub-mm structures. The experimental data reveals that even at the small dissipative scales, peak mixing does not occur in overturns (bright cores), but in thin, relatively flat, sheared filaments, where χ_s exceeds the braid-average by two orders of magnitude. Because the experiment shown operated at the lower end of the expected braid $\mathrm{Re_b}$, the separation between braid and filament scales in the field – and the associated mixing levels – should be even sharper than visualized here.

7 Implications

The first implication of these results concerns the qualitative structure of density interfaces in high-Re, forced environments. Even under vigorous shear instabilities, estuarine pycnoclines rarely show steps; instead they remain close to a smooth, hyperbolic-tangent form. A step-like structure with a central mixed layer would be expected if mixing were dominated by large overturns in the billow cores, as in lower-Re, unforced flows. Instead, smaller-scale braid and eyelid mixing along the flanks of billows continually entrains fluid at the edges of the pycnocline, broadening the interface smoothly without ever carving out a central mixed layer. Future work should estimate what fraction of global ocean mixing occurs in this high-Re, forced regime; the gallery of observations in Appendix A suggests this fraction could be significant.

The second implication concerns mixing efficiency Γ and how closures represent $\mathrm{Ri_g}$-dependent stability functions. We revealed a sustained baroclinic production–dissipation balance with local $\mathrm{Ri_g} \approx \Gamma \approx 0.1$–$0.15$ at both the main pycnocline and the finer braid scales, below the canonical $\mathrm{Ri_g} = 0.25$ and $\Gamma = 0.2$ (Gregg et al., 2018; Holleman et al., 2016). These lower values, however, may not represent the event-integrated mixing of the primary KH train. If the averaging aperture is widened to include the full pycnocline and primary instability lifecycle – as may be more typical of available model resolution – $\mathrm{Ri_g}$ and Γ may rise toward the canonical values, so the bulk Γ may be more reflective of the marginal $\mathrm{Ri_g}$ that triggers the instability than the local submarginal $\mathrm{Ri_g}$ at peak shear and mixing. Closures for continuously forced mixing hotspots may need to account for such a resolution-dependence of stability threshold and mixing efficiency.

The third implication, which is related, concerns how dissipation and mixing are predicted and interpreted across scales in field observations. Our baroclinic production–dissipation balance provide practical predications for pycnocline- and braid-scale ϵ and χ from local slope, velocity, and length scales. Yet these averages integrate over myriad extreme filaments beyond the reach of microstructure and micro-CTD profilers, raising the question of what is actually being averaged over in field data, depending on their spatio-temporal resolution. Our results also suggest that the fine-scale cascade remains Re-dependent even at very high Re.

Acknowledgements

We thank C. P. Caulfield, S. F. Lewin and E. R. Bouckley for discussions on secondary KH instability at the WHOI Geophysical Fluid Dynamics Program supported by the NSF and ONR. Computing was performed on the Delta HPC at the University of Illinois Urbana-Champaign, supported by the NSF and the State of Illinois. Lefauve was supported by a NERC Independent Research Fellowship NE/W008971/1. Bassett, Plotnick, Lavery and Geyer were supported by ONR Grants N00014-16-1-2948 and N00014-19-1-2593. ChatGPT (OpenAI) was used for minor language editing.

Data Availability

All data supporting the conclusions of this study – including multibeam movies corresponding to transects T1-T3 – will be made publicly available upon publication via a public repository (to be specified).

Conflict of Interest

The authors declare no conflicts of interest.

Appendix A Gallery of field observations of KH instabilities

Figure A1 gives an overview of KH visualizations around the world's oceans, reproducing snapshots from the literature and personal communication. Most cases were captured with single-beam echosounders; the deeper-ocean examples (panels l, m, and u) used thermistor arrays, and panel (d) is an early multibeam record. The details of some of these observations are tabulated in (Tu et al., 2020, Table 1). Although the direction of the shear varied among studies – and thus the left-right orientation of the braids – here we flipped them to be consistent with our convention ($\partial U/\partial z > 0$ and braid slope $\alpha > 0$). The only exception is the lower image in panel (j), where two trains of instabilities formed simultaneously on stacked pycnoclines with shear in opposite directions. Note that in all panels (except d), the lack of multibeam imagery means true braid slopes and aspect ratios are unknown and typically appear exaggerated, due to inevitable acquisition distortion and arbitrary scaling in these space–time plots.

Three key points emerge from figure A1. First, the KH instability is a ubiquitous mixing process, occurring in a variety of environments, depths, and modes of stratification, including:

- **salinity stratification (pycnoclines)** in estuaries and straits, such as in panels (a-c) the Connecticut River salt-wedge estuary (Geyer et al., 2010; Lavery et al., 2013; Holleman et al., 2016); (d) the Knight inlet, a tidally driven fjord (Colbo et al., 2014); (e,f) the Fraser River estuary (Geyer & Smith, 1987; Tedford et al., 2009); (h) the Admiralty inlet (Seim & Gregg, 1994); (i) the Columbia River estuary (Lavery, A. C., Personal Communication, 2023); (j) the Mobile Bay estuary (Bassett, C., Personal Communication, 2021); (k) the James River estuary (Bassett et al., 2023); (n) the Strait of Gibraltar (Wesson & Gregg, 1994) and (r) the Kuroshio intrusion into the Changjiang River plume (Tu et al., 2024);
- **temperature stratification (thermoclines)**, such as in (g) the Oregon continental shelf (Moum et al., 2003); (o) the Gulf Stream along the New England shelf break (disregarding the small-scale, uncorrected fluctuations of the braid from the heave of the boat; Zhang, G. & Lavery, A. C., Personal Communication, 2016); (l) the deep downslope channel flow of Antarctic Bottom Water through the Romanche Trench (displaying buoyancy frequency N) (van Haren et al., 2014); (m) the tidally driven downslope flow above Great Meteor

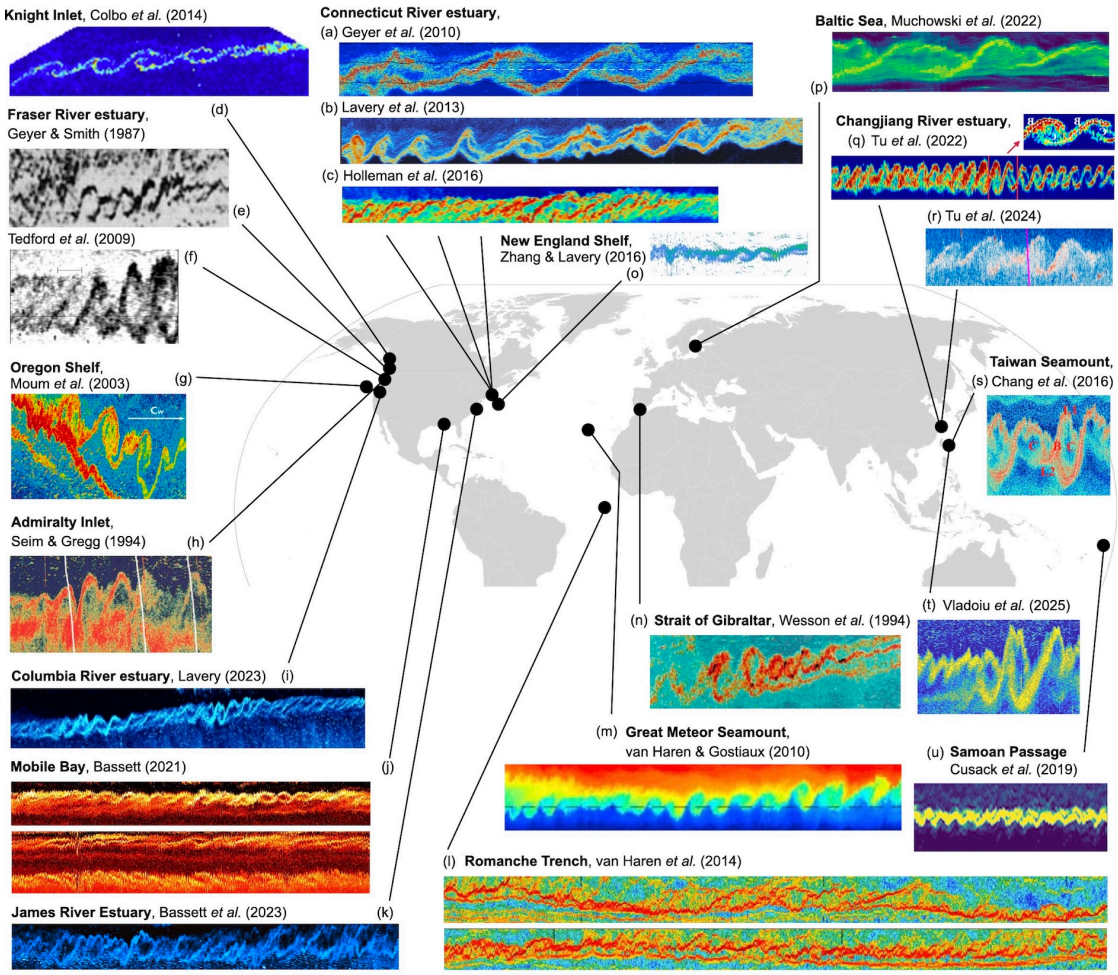

Figure A1. Visualizations of KH instabilities, showing the wide relevance of braid-driven mixing in hotspots with continuous shear forcing, with the possible exception of a more transient internal wave overturn in (g). Adapted with permission from the authors. See main text for details and references.

Seamount (displaying temperature) (van Haren & Gostiaux, 2010); (p) the northern Baltic Sea above a sill (Muchowski et al., 2022); (s,t) the Kuroshio above a seamount off south-eastern Taiwan (M. Chang et al., 2016; Vladoiu et al., 2025); (u) the deep overflow in the Samoan Passage (Cusack et al., 2019);

- **sediment-induced stratification (lutoclines)** in highly turbid estuaries such as in (q) the Changjiang river (Tu et al., 2022).

Second, KH billows occur across a wide range of scales, with vertical amplitudes spanning three orders of magnitude: from $\delta \approx 0.5$–2 m in shallow estuaries (a–c, e,f, q,r, and j), to 5–20 m in deeper estuaries and coastal flows (d, g–i, k, and p), and to 50–200 m in the Strait of Gibraltar (n) and in the open ocean (l-m, and s-u). Typical velocity scales vary much less, and tend to be of order $\Delta U \sim 1\,\mathrm{m\,s^{-1}}$ across studies. This implies a range of Reynolds numbers $\mathrm{Re} \sim 10^5 - 10^7$, with turbulence likely triggered by secondary instabilities at the lower Re (coastal ocean) and by tertiary instabilities at the higher Re (deep ocean).

Third, the typical structure of high-Re mixing observed and explained in this paper – 'bright' baroclinic braids connecting quiet 'dark' cores – appears generic. The notable exception is the

internal solitary wave propagating shoreward over the Oregon shelf (panel g), where the primary billow overturns and mixes significantly. We attribute this to the transient, time-dependent shear and steepening of solitary waves, in contrast with the more steady shear forcing assumed in our braid-mixing model and dominant in other observations.

Appendix B Numerical simulation method

The 2D DNS presented in Sec. 5.1 were performed with the Julia package `Oceananigans.jl` (Ramadhan et al., 2020). The base state consists of hyperbolic-tangent velocity and salinity profiles inspired by the field profiles of figure 7:

$$u(z,0) = 0.5\tanh(2z)\,\mathrm{m\,s^{-1}}, \qquad s(z,0) = 13 - 10\tanh(2z)\,\mathrm{psu}, \tag{B1}$$

with buoyancy $b = g\beta(13 - s)$ over a vertical domain $z \in [-2.5, 2.5]\,\mathrm{m}$ (total depth 5 m). These dimensional forms is shown for clarity and correspond to the results plotted in figure 15

The simulation solved the incompressible, non-hydrostatic Navier–Stokes equations under the Boussinesq approximation, given in dimensionless form by

$$\tilde{\nabla}\cdot\tilde{\mathbf{u}} = 0, \qquad \frac{\partial\tilde{\mathbf{u}}}{\partial\tilde{t}} + \tilde{\mathbf{u}}\cdot\tilde{\nabla}\mathbf{u} = -\tilde{\nabla}\tilde{p} + \frac{1}{\mathrm{Re}}\tilde{\nabla}^2\tilde{\mathbf{u}} + Ri\,\tilde{b}\,\mathbf{e}_z, \qquad \frac{\partial\tilde{b}}{\partial\tilde{t}} + \tilde{\mathbf{u}}\cdot\tilde{\nabla}\tilde{b} = \frac{1}{\mathrm{Re\,Sc}}\tilde{\nabla}^2\tilde{b}, \tag{B2}$$

with parameters $(\mathrm{Re}, \mathrm{Ri}, \mathrm{Sc})$ given by Eq. (9). The solver used finite-volume discretization, WENO advection, and third-order Runge–Kutta timestepping on an Nvidia A100 GPU (40 GB).

Free-slip and no-flux boundary conditions were imposed at the top and bottom, and periodic boundary conditions were applied in x. Although figure 15 shows two wavelengths for clarity, only a single wavelength was simulated, which is sufficient since vortex pairing is irrelevant at the high Re considered.

An initial perturbation was imposed as the fastest-growing linear mode (wavelength 6.5 m) with energy (defined as the domain-averaged $(1/2)(u^2 + w^2 + b^2)$) equal to 10^{-4} of the base flow, plus white noise with energy equal to 10^{-3} of the base flow – still moderate compared to expected field levels.

A stretched vertical grid ($10^4 \times 10^4$ points in x and z) was used to capture sharp gradients at the braid scale and ensure convergence. In physical units, the horizontal grid spacing was $\Delta x = 0.65\,\mathrm{mm}$, the vertical spacing averaged $\Delta z = 0.5\,\mathrm{mm}$, and reached a minimum $\Delta z = 0.25\,\mathrm{mm}$ at $z = 0$.

References

Bak, P., Tang, C., & Wiesenfeld, K. (1988). Self-organized criticality. *Phys. Rev. A*, *38*(1), 364.

Bartello, P., & Tobias, S. M. (2013). Sensitivity of stratified turbulence to the buoyancy Reynolds number. *J. Fluid Mech.*, *725*, 1–22. doi: 10.1017/jfm.2013.170

Bassett, C., Lavery, A. C., Petitt, R., & Loranger, S. (2022). Autonomous platforms for measuring broadband backscatter. *Proc. Meet. Acoust.*, *45*(1), 005002. doi: 10.1121/2.0001654

Bassett, C., Lavery, A. C., Ralston, D., Geyer, W. R., Jurisa, J. T., Thomson, J., ... Haller, M. C. (2023). Acoustic backscattering at a tidal intrusion front. *Prog. Oceanogr.*, *219*, 103167. doi: 10.1016/j.pocean.2023.103167

Carpenter, J. R., Tedford, E. W., Rahmani, M., & Lawrence, G. A. (2010). Holmboe wave fields in simulation and experiment. *J. Fluid Mech.*, *648*, 205–223. doi: 10.1017/S002211200999317X

Caulfield, C. P. (1994). Multiple linear instability of layered stratified shear flow. *J. Fluid Mech.*, *258*, 255–285.

Caulfield, C. P. (2020). Open questions in turbulent stratified mixing: Do we even know what we do not know? *Phys. Rev. Fluids*, *5*, 110518.

Caulfield, C. P. (2021). Layering, instabilities, and mixing in turbulent stratified flows. *Ann. Rev. Fluid Mech.*, *53*, 113–145.

Caulfield, C. P., & Peltier, W. R. (2000). The anatomy of the mixing transition in homogeneous and stratified free shear layers. *J. Fluid Mech.*, *413*, 1–47.

Chang, M., Jheng, S., & Lien, R. (2016). Trains of large Kelvin-Helmholtz billows observed in the Kuroshio above a seamount. *Geophys. Res. Lett.*, *43*(16), 8654–8661. doi: 10.1002/2016GL069462

Chang, M.-H. (2021). Marginal instability within internal solitary waves. *Geophys. Res. Lett.*, *48*(9), e2021GL092616. doi: 10.1029/2021GL092616

Cimoli, L., Mashayek, A., Johnson, H. L., Marshall, D. P., Naveira Garabato, A. C., Whalen, C. B., ... Talley, L. D. (2023). Significance of Diapycnal Mixing Within the Atlantic Meridional Overturning Circulation. *AGU Advances*, *4*(2), e2022AV000800. doi: 10.1029/2022AV000800

Colbo, K., Ross, T., Brown, C., & Weber, T. (2014). A review of oceanographic applications of water column data from multibeam echosounders. *Est. Coast. Shelf Sci.*, *145*, 41–56. doi: 10.1016/j.ecss.2014.04.002

Corcos, G. M., & Sherman, F. S. (1976). Vorticity concentration and the dynamics of unstable free shear layers. *J. Fluid Mech.*, *73*(02), 241–264. doi: 10.1017/S0022112076001365

Cusack, J. M., Voet, G., Alford, M. H., Girton, J. B., Carter, G. S., Pratt, L. J., ... Tan, S. (2019). Persistent Turbulence in the Samoan Passage. *J. Phys. Oceanogr.*, *49*(12), 3179–3197. doi: 10.1175/JPO-D-19-0116.1

Dritschel, D. G., Haynes, P. H., Juckes, M. N., & Shepherd, T. G. (1991). The stability of a two-dimensional vorticity filament under uniform strain. *J. Fluid Mech.*, *230*, 647–665. doi: 10.1017/S0022112091000826

D'Asaro, E. A. (2022). How do internal waves create turbulence and mixing in the ocean? [preprint]. *ESS Open Archive*.

Geyer, W. R., Lavery, A. C., Scully, M. E., & Trowbridge, J. H. (2010). Mixing by shear instability at high Reynolds number. *Geophys. Res. Lett.*, *37*(22), 2010GL045272. doi: 10.1029/2010GL045272

Geyer, W. R., Ralston, D. K., & Holleman, R. C. (2017). Hydraulics and mixing in a laterally divergent channel of a highly stratified estuary. *J. Geophys. Res. Oceans*, *122*(6), 4743–4760. doi: 10.1002/2016JC012455

Geyer, W. R., Scully, M. E., & Ralston, D. K. (2008). Quantifying vertical mixing in estuaries. *Environ. Fluid Mech.*, *8*(5-6), 495–509. doi: 10.1007/s10652-008-9107-2

Geyer, W. R., & Smith, J. (1987). Shear instability of a highly stratified estuary. *J. Phys. Oceanogr.*, *17*, 1668–1679.

Gregg, M. C., D'Asaro, E. A., Riley, J. J., & Kunze, E. (2018). Mixing efficiency in the ocean. *Ann. Rev. Mar. Sci.*, *10*, 443–473.

Hasegawa, D., Matsuno, T., Tsutsumi, E., Senjyu, T., Endoh, T., Tanaka, T., ... Guo, X. (2021). How a small reef in the Kuroshio cultivates the ocean. *Geophys. Res. Lett.*, *48*(7), e2020GL092063. doi: 10.1029/2020GL092063

Hazel, P. (1972). Numerical studies of the stability of inviscid stratified shear flows. *J. Fluid Mech.*, *51*(01), 39–61.

Hoecker-Martínez, M. S., & Smyth, W. D. (2012). Trapping of gyrotactic organisms in an unstable shear layer. *Cont. Shelf Res.*, *36*, 8–18. doi: 10.1016/j.csr.2012.01.003

Holleman, R. C., Geyer, W. R., & Ralston, D. K. (2016). Stratified Turbulence and Mixing Efficiency in a Salt Wedge Estuary. *J. Phys. Oceanogr.*, *46*(6), 1769–1783. doi: 10.1175/JPO-D-15-0193.1

Howard, L. N. (1961). Note on a paper of John W. Miles. *J. Fluid Mech.*, *10*(04), 509. doi: 10.1017/S0022112061000317

Jackson, P. R., & Rehmann, C. R. (2014). Experiments on Differential Scalar Mixing in Turbulence in a Sheared, Stratified Flow. *J. Phys. Oceanogr.*, *44*(10), 2661–2680. doi: 10.1175/JPO-D-14-0027.1

Klaassen, G. P., & Peltier, W. R. (1985). The onset of turbulence in finite-amplitude Kelvin–Helmholtz billows. *J. Fluid Mech.*, *155*, 1–35. doi: 10.1017/S0022112085001721

Klaassen, G. P., & Peltier, W. R. (1989). The role of transverse secondary instabilities in the evolution of free shear layers. *J. Fluid Mech.*, *202*, 367–402. doi: 10.1017/S0022112089001210

Klaassen, G. P., & Peltier, W. R. (1991). The influence of stratification on secondary instability in free shear layers. *J. Fluid Mech.*, *227*, 71–106. doi: 10.1017/S0022112091000013

Kundu, P. K., Cohen, I. M., & Dowling, D. R. (2016). *Fluid Mechanics* (6th ed.). Elsevier.

Lavery, A. C., Geyer, W. R., & Scully, M. E. (2013). Broadband acoustic quantification of stratified turbulence. *J. Acoust. Soc. Am.*, *134*(1), 40–54. doi: 10.1121/1.4807780

Lefauve, A. (2024). Geophysical stratified turbulence and mixing in the laboratory. *C. R. Phys.*, *25*(no. S3), no. S3, 1–29. doi: 10.5802/crphys.196

Lefauve, A., & Linden, P. F. (2020). Buoyancy-driven exchange flows in inclined ducts. *J. Fluid Mech.*, *893*, A2.

Lefauve, A., & Linden, P. F. (2022a). Experimental properties of continuously forced, shear-driven, stratified turbulence. Part 1. Mean flows, self-organisation, turbulent fractions. *J. Fluid Mech.*, *937*, A34.

Lefauve, A., & Linden, P. F. (2022b). Experimental properties of continuously forced, shear-driven, stratified turbulence. Part 2. Energetics, anisotropy, parameterisation. *J. Fluid Mech.*, *937*, A35.

Liu, Z., Hu, S., Zhang, R., Li, Y., Chen, D., Yang, D., ... Lin, X. (2025). Subsurface turbulent mixing generates a positive feedback to Central Pacific ENSO. *Nat. Comm.*, *16*, 3035. doi: 10.1038/s41467-025-56477-6

Mashayek, A., & Peltier, W. R. (2011). Turbulence transition in stratified atmospheric and oceanic shear flows: Reynolds and Prandtl number controls upon the mechanism. *Geophys. Res. Lett.*, *38*, L16612. doi: 10.1029/2011GL048542

Mashayek, A., & Peltier, W. R. (2012a). The 'zoo' of secondary instabilities precursory to stratified shear flow transition. Part 1: Shear aligned convection, pairing, and braid instabilities. *J. Fluid Mech.*, *708*, 5–44. doi: 10.1017/jfm.2012.304

Mashayek, A., & Peltier, W. R. (2012b). The 'zoo' of secondary instabilities precursory to stratified shear flow transition. Part 2: The influence of stratification. *J. Fluid Mech.*, *708*, 45–70. doi: 10.1017/jfm.2012.294

Melet, A. V., Hallberg, R., & Marshall, D. P. (2022). The role of ocean mixing in the climate system. In *Ocean Mixing* (pp. 5–34). Elsevier. doi: 10.1016/B978-0-12-821512-8.00009-8

Melvin, G., Fox, P. A., & Condiotty, J. (2012, July). Adaption of the M3 multi-beam sonar to fisheries applications. In *Proc. Meet. Acoust.* (Vol. 17, p. 070031). Acoust. Soc. Am. doi: 10.1121/1.4772777

Meyer, C. R., & Linden, P. F. (2014). Stratified shear flow: experiments in an inclined duct. *J. Fluid Mech.*, *753*, 242–253. doi: 10.1017/jfm.2014.358

Miles, J. W. (1961). On the stability of heterogeneous shear flows. *J. Fluid Mech.*, *10*(4), 496–508.

Moum, J. N., Farmer, D. M., Smyth, W. D., Armi, L., & Vagle, S. (2003). Structure and gener-

ation of turbulence at interfaces strained by internal solitary waves propagating shoreward over the continental shelf. *J. Phys. Oceanogr.*, *33*, 2093–2112.

Muchowski, J., Umlauf, L., Arneborg, L., Holtermann, P., Weidner, E., Humborg, C., & Stranne, C. (2022). Potential and Limitations of a Commercial Broadband Echo Sounder for Remote Observations of Turbulent Mixing. *J. Atmos. Oceanic Technol.*, *39*(12), 1985–2003. doi: 10.1175/JTECH-D-21-0169.1

Partridge, J. L., Lefauve, A., & Dalziel, S. B. (2019). A versatile scanning method for volumetric measurements of velocity and density fields. *Meas. Sci. Tech.*, *30*, 055203.

Petropoulos, N., Couchman, M. M., Mashayek, A., De Bruyn Kops, S. M., & Caulfield, C.-c. P. (2024). Prandtl number effects on extreme mixing events in forced stratified turbulence. *J. Fluid Mech.*, *983*, R1. doi: 10.1017/jfm.2024.110

Portwood, G. D., de Bruyn Kops, S. M., & Caulfield, C. P. (2019). Asymptotic dynamics of high dynamic range stratified turbulence. *Phys. Rev. Lett.*, *122*, 194504.

Ramadhan, A., Wagner, G. L., Hill, C., Campin, J.-M., Churavy, V., Besard, T., ... Marshall, J. (2020). Oceananigans.jl: Fast and friendly geophysical fluid dynamics on GPUs. *J. Open Source Softw.*, *5*(53), 2018. doi: 10.21105/joss.02018

Riley, J. J., & Lindborg, E. (2008). Stratified turbulence: A possible interpretation of some geophysical turbulence measurements. *J. Atmos. Sci.*, *65*(7), 2416–2424. doi: 10.1175/2007JAS2455.1

Salehipour, H., Peltier, W. R., & C. P. Caulfield, C. P. (2018). Self-organized criticality of turbulence in strongly stratified mixing layers. *J. Fluid Mech.*, *856*, 228–256.

Seim, H. E., & Gregg, M. C. (1994). Detailed observations of a naturally occurring shear instability. *J. Geophys. Res. Oceans*, *99*(C5), 10049–10073. doi: 10.1029/94JC00168

Simpson, J. H., & Nunes, R. A. (1981). The tidal intrusion front: An estuarine convergence zone. *Estuarine, Coastal and Shelf Science*, *13*, 257–266. doi: 10.1016/S0302-3524(81)80024-2

Smyth, W. D. (2003). Secondary Kelvin–Helmholtz instability in weakly stratified shear flow. *J. Fluid Mech.*, *497*, 67–98. doi: 10.1017/S0022112003006591

Smyth, W. D. (2020). Marginal Instability and the Efficiency of Ocean Mixing. *J. Phys. Oceanogr.*, *50*(8), 2141–2150. doi: 10.1175/JPO-D-20-0083.1

Smyth, W. D., & Carpenter, J. R. (2019). *Instability in Geophysical Flows* (1st ed.). Cambridge University Press. doi: 10.1017/9781108640084

Smyth, W. D., & Moum, J. N. (2000). Length scales of turbulence in stably stratified mixing layers. *Phys. Fluids*, *12*(6), 1327–1342. doi: 10.1063/1.870385

Smyth, W. D., & Moum, J. N. (2012). Ocean mixing by Kelvin-Helmholtz instability. *Oceanography*, *25*(2), 140–149. doi: 10.5670/oceanog.2012.48

Smyth, W. D., & Moum, J. N. (2013). Marginal instability and deep cycle turbulence in the eastern equatorial Pacific Ocean. *Geophys. Res. Lett.*, *40*(23), 6181–6185. doi: 10.1002/2013GL058403

Smyth, W. D., Moum, J. N., Li, L., & Thorpe, S. A. (2013). Diurnal shear instability, the descent of the surface shear layer, and the deep cycle of equatorial turbulence. *J. Phys. Oceanogr.*, *43*(11), 2432–2455. doi: 10.1175/JPO-D-13-089.1

Staquet, C. (1995). Two-dimensional secondary instabilities in a strongly stratified shear layer. *J. Fluid Mech.*, *296*, 73–126. doi: 10.1017/S0022112095002080

Steinbuck, J. V., Stacey, M. T., McManus, M. A., Cheriton, O. M., & Ryan, J. P. (2009). Observations of turbulent mixing in a phytoplankton thin layer: Implications for formation, maintenance, and breakdown. *Limnol. Oceanogr.*, *54*(4), 1353–1368. doi: 10.4319/lo.2009.54.4.1353

Taylor, J. R., & Thompson, A. F. (2023). Submesoscale dynamics in the upper ocean. *Ann. Rev. Fluid Mech.*, *55*, 103–127. doi: 10.1146/annurev-fluid-031422-095147

Tedford, E. W., Carpenter, J. R., Pawlowicz, R., Pieters, R., & Lawrence, G. A. (2009). Observation and analysis of shear instability in the Fraser River estuary. *J. Geophys. Res. Oceans*, *114*, C11006.

Thorpe, S. A. (1971). Experiments on the instability of stratified shear flows: miscible fluids. *J. Fluid Mech.*, *46*(02), 299–319.

Thorpe, S. A. (1973). Experiments on instability and turbulence in a stratified shear flow. *J. Fluid Mech.*, *61*(04), 731–751. doi: 10.1017/S0022112073000911

Thorpe, S. A., & Liu, Z. (2009). Marginal Instability? *J. Phys. Oceanogr.*, *39*(9), 2373–2381. doi: 10.1175/2009JPO4153.1

Tu, J., Fan, D., Lian, Q., Liu, Z., Liu, W., Kaminski, A., & Smyth, W. (2020). Acoustic Observations of Kelvin-Helmholtz Billows on an Estuarine Lutocline. *J. Geophys. Res. Oceans*, *125*(4), e2019JC015383. doi: 10.1029/2019JC015383

Tu, J., Fan, D., Sun, F., Kaminski, A., & Smyth, W. (2022). Shear Instabilities and Stratified Turbulence in an Estuarine Fluid Mud. *J. Phys. Oceanogr.*, *52*(10), 2257–2271. doi: 10.1175/JPO-D-21-0230.1

Tu, J., Wu, J., Fan, D., Liu, Z., Zhang, Q., & Smyth, W. (2024). Shear Instability and Turbulent Mixing by Kuroshio Intrusion Into the Changjiang River Plume. *Geophys. Res. Lett.*, *51*(20), e2024GL110957. doi: 10.1029/2024GL110957

van Haren, H., & Gostiaux, L. (2010). A deep-ocean Kelvin-Helmholtz billow train. *Geophys. Res. Lett.*, *37*(3), L03605. doi: 10.1029/2009GL041890

van Haren, H., Gostiaux, L., Morozov, E., & Tarakanov, R. (2014). Extremely long Kelvin-Helmholtz billow trains in the Romanche Fracture Zone. *Geophys. Res. Lett.*, *41*(23), 8445–8451.

Vladoiu, A., Lien, R.-C., Kunze, E., Ma, B., Essink, S., Yang, Y. J., ... Yeh, Y.-Y. (2025). Finescale measurements of Kelvin-Helmholtz instabilities at a kuroshio seamount. *J. Phys. Oceanogr.*. (in press) doi: 10.1175/JPO-D-24-0235.1

Waterhouse, A. F., MacKinnon, J. A., Nash, J. D., Alford, M. H., Kunze, E., Simmons, H. L., ... Lee, C. M. (2014). Global patterns of diapycnal mixing from measurements of the turbulent dissipation rate. *J. Phys. Oceanogr.*, *44*(7), 1854–1872. doi: 10.1175/JPO-D-13-0104.1

Wenegrat, J. O., & McPhaden, M. J. (2015). Dynamics of the surface layer diurnal cycle in the equatorial Atlantic Ocean (0°, 23°W). *J. Geophys. Res. Oceans*, *120*(1), 563–581. doi: 10.1002/2014JC010504

Wesson, J. C., & Gregg, M. C. (1994). Mixing at Camarinal sill in the strait of Gibraltar. *J. Geophys. Res. Oceans*, *99*, 9847–9878.

Zhu, L., Atoufi, A., Lefauve, A., Taylor, J. R., Lawrence, G. A., Dalziel, S. B., ... Linden, P. F. (2023). Stratified inclined duct: direct numerical simulations. *J. Fluid Mech.*, *969*, A20.